The Astrophysical Journal, 666:870–895, 2007 September 10

THE CALIBRATION OF MID-INFRARED STAR FORMATION RATE INDICATORS[1]

D. Calzetti,[2,3] R. C. Kennicutt,[4] C. W. Engelbracht,[5] C. Leitherer,[3] B. T. Draine,[6] L. Kewley,[7]
J. Moustakas,[8] M. Sosey,[3] D. A. Dale,[9] K. D. Gordon,[5] G. X. Helou,[10] D. J. Hollenbach,[11]
L. Armus,[10] G. Bendo,[12] C. Bot,[10] B. Buckalew,[10] T. Jarrett,[10] A. Li,[13] M. Meyer,[3]
E. J. Murphy,[14] M. Prescott,[5] M. W. Regan,[3] G. H. Rieke,[5] H. Roussel,[15]
K. Sheth,[10] J. D. T. Smith,[5] M. D. Thornley,[16] and F. Walter[15]

Received 2007 May 1; accepted 2007 May 22

ABSTRACT

With the goal of investigating the degree to which the MIR emission traces the SFR, we analyze *Spitzer* 8 and 24 μm data of star-forming regions in a sample of 33 nearby galaxies with available *HST* NICMOS images in the Paα (1.8756 μm) emission line. The galaxies are drawn from the SINGS sample and cover a range of morphologies and a factor $\sim$10 in oxygen abundance. Published data on local low-metallicity starburst galaxies and LIRGs are also included in the analysis. Both the stellar continuum–subtracted 8 μm emission and the 24 μm emission correlate with the extinction-corrected Paα line emission, although neither relationship is linear. Simple models of stellar populations and dust extinction and emission are able to reproduce the observed nonlinear trend of the 24 μm emission versus number of ionizing photons, including the modest deficiency of 24 μm emission in the low-metallicity regions, which results from a combination of decreasing dust opacity and dust temperature at low luminosities. Conversely, the trend of the 8 μm emission as a function of the number of ionizing photons is not well reproduced by the same models. The 8 μm emission is contributed, in larger measure than the 24 μm emission, by dust heated by nonionizing stellar populations, in addition to the ionizing ones, in agreement with previous findings. Two SFR calibrations, one using the 24 μm emission and the other using a combination of the 24 μm and Hα luminosities (Kennicutt and coworkers), are presented. No calibration is presented for the 8 μm emission because of its significant dependence on both metallicity and environment. The calibrations presented here should be directly applicable to systems dominated by ongoing star formation.

Subject headings: galaxies: interactions — galaxies: ISM — galaxies: starburst — ISM: structure

1. INTRODUCTION

The multiwavelength galaxy surveys of unprecedented angular resolution recently made available by combined space (*Hubble Space Telescope* [*HST*], *Spitzer*) and ground-based observations are providing for the first time the tools to cross calibrate star formation rate (SFR) indicators at different wavelengths and to test the physical assumptions underlying each indicator.

Easy accessibility has traditionally favored the use of the ultraviolet (UV) stellar continuum and of the optical nebular recombination lines as SFR indicators, the former mainly in the intermediate- to high-redshift regime (as it gets redshifted into the optical observer frame) and the latter mostly in low-redshift surveys. Both indicators only probe the stellar light that *emerges from a galaxy unabsorbed by dust*. The UV is heavily affected by dust attenuation, and numerous efforts have attempted to find general tools to mitigate the effects of dust on this important SFR indicator (e.g., Calzetti et al. 1994; Kennicutt 1998b; Meurer et al. 1999; Hopkins et al. 2001; Sullivan et al. 2001; Buat et al. 2002, 2005; Bell 2003; Hopkins 2004; Salim et al. 2007). Cross calibrations with optical recombination lines and other indicators have also attempted to account for the $\sim$10 times or more longer stellar timescales probed by the UV relative to tracers of ionizing photons (e.g., Sullivan et al. 2001; Kong et al. 2004; Calzetti et al. 2005). Among the recombination lines, Hα is the most widely used, due to a combination of its intensity and a lower sensitivity to dust attenuation than bluer nebular lines. Although to a much lesser degree than the UV, the Hα line is still affected by dust attenuation, plus it is impacted by assumptions on the underlying stellar absorption and on the form of the high end of the stellar initial mass function (IMF; e.g., Calzetti et al. 1994; Kennicutt 1998b; Hopkins et al. 2001; Sullivan et al. 2001; Kewley et al. 2002; Rosa-Gonzalez et al. 2002).

Infrared SFR indicators are complementary to UV–optical indicators because they measure star formation via the dust-absorbed stellar light that emerges beyond a few microns. Although SFR indicators using the infrared emission had been calibrated during the *IRAS* times (e.g., Lonsdale Persson &

[1] Based on observations obtained with the *Spitzer Space Telescope*, which is operated by JPL, Caltech, under NASA contract 1407, and with the NASA/ESA *Hubble Space Telescope* at the Space Telescope Science Institute, which is operated by the Association of Universities for Research in Astronomy, Inc., under NASA contract NAS5-26555.
[2] Department of Astronomy, University of Massachusetts, Amherst, MA 01003; calzetti@astro.umass.edu.
[3] Space Telescope Science Institute, Baltimore, MD 21218.
[4] Institute of Astronomy, Cambridge University, Cambridge CB3 0HA, UK.
[5] Steward Observatory, University of Arizona, Tucson, AZ 85721.
[6] Princeton University Observatory, Princeton, NJ 08544.
[7] Institute for Astronomy, University of Hawaii, Honolulu, HI 96822.
[8] Department of Physics, New York University, New York, NY 10003.
[9] Department of Physics and Astronomy, University of Wyoming, Laramie, WY 82071.
[10] *Spitzer* Science Center, California Institute of Technology, Pasadena, CA 91125.
[11] NASA/Ames Research Center, Moffett Field, CA 94035.
[12] Astrophysics Group, Imperial College of Science, Technology, and Medicine, London SW7 2AZ, UK.
[13] Department of Physics and Astronomy, University of Missouri, Columbia, MO 65211.
[14] Department of Astronomy, Yale University, New Haven, CT 06520.
[15] Max-Planck-Institut für Astronomie, Heidelberg D-69117, Germany.
[16] Department of Physics and Astronomy, Bucknell University, Lewisburg, PA 17837.

Helou 1987; Rowan-Robinson & Crawford 1989; Sauvage & Thuan 1992), interest in this wavelength range had been rekindled in more recent times by the discovery of submillimeter-emitting galaxy populations at cosmological distances (e.g., Smail et al. 1997; Hughes et al. 1998; Barger et al. 1998; Eales et al. 1999; Chapman et al. 2005). In dusty starburst galaxies, the bolometric infrared luminosity L_{IR} in the $\sim$3–1100 μm window is directly proportional to the SFR (e.g., Kennicutt 1998b). However, even assuming that most of the luminous energy produced by recently formed stars is reprocessed by dust in the infrared, at least two issues make the use of this SFR indicator problematic: (1) evolved, i.e., non-star-forming, stellar populations also heat the dust that emits in the IR wavelength region, thus affecting the calibration of SFR(IR) in a stellar population–dependent manner (e.g., Lonsdale Persson & Helou 1987; Helou 1986; Kennicutt 1998b); and (2) in intermediate/high-redshift studies, the bolometric infrared luminosity is often extrapolated from measurements at sparsely sampled wavelengths, most often in the submillimeter and radio observer's frame (e.g., Smail et al. 1997; Chapman et al. 2005), and such extrapolations are subject to many uncertainties.

The interest in calibrating monochromatic mid-infrared (MIR) SFR diagnostics stems from their potential application to both the local universe and intermediate- and high-redshift galaxies observed with *Spitzer* and future infrared/submillimeter missions (Daddi et al. 2005; Wu et al. 2005). One such application is the investigation of the scaling laws of star formation in the dusty environments of galactic centers (Kennicutt 1998a; Kennicutt et al. 2007). The use of monochromatic (i.e., one band or wavelength) infrared emission for measuring SFRs offers one definite advantage over the bolometric infrared luminosity: it removes the need for highly uncertain extrapolations of the dust spectral energy distribution (SED) across the full wavelength range. Over the last few years, a number of efforts have gone into investigating the potential use of monochromatic infrared emission for measuring SFRs.

Early studies employing *Infrared Space Observatory* (*ISO*) data have not resolved whether the warm dust and aromatic band emission around 8 μm can be effectively used as an SFR indicator, since different conclusions have been reached by different authors. Roussel et al. (2001) and Förster Schreiber et al. (2004) have shown that the emission in the 6.75 μm *ISO* band correlates with the number of ionizing photons (SFR) in galaxy disks and in the nuclear regions of galaxies. Conversely, Boselli et al. (2004) have found that the MIR emission in a more diverse sample of galaxies (types Sa through Im-BCDs) correlates more closely with tracers of evolved stellar populations not linked to the current star formation. In addition, Haas et al. (2002) find that the *ISO* 7.7 μm emission is correlated with the 850 μm emission from galaxies, suggesting a close relation between the *ISO* band emission and the cold dust heated by the general (non-star-forming) stellar population. This divergence of results highlights the multiplicity of sources for the emission at 8 μm (e.g., Peeters et al. 2004; Tacconi-Garman et al. 2005), as well as the limits in the *ISO* angular resolution and sensitivity for probing a sufficiently wide range of galactic conditions.

The emission in the 8 μm and other MIR bands is generally attributed to polycyclic aromatic hydrocarbons (PAHs; Leger & Puget 1984; Sellgren 1984; Allamandola et al. 1985; Sellgren et al. 1990), large molecules transiently heated by single UV and optical photons in the general radiation field of galaxies or near B stars (Li & Draine 2002; Haas et al. 2002; Boselli et al. 2004; Peeters et al. 2004; Wu et al. 2005; Mattioda et al. 2005), which can be destroyed, fragmented, or ionized by harsh UV photon fields (Boulanger et al. 1988, 1990; Helou et al. 1991; Houck et al. 2004; Pety et al. 2005). *Spitzer* data of the nearby galaxies NGC 300 and NGC 4631 show that 8 μm emission highlights the rims of H II regions and is depressed inside the regions, indicating that the PAH dust is heated in the photodissociation regions (PDRs) surrounding H II regions and is destroyed within the regions (Helou et al. 2004; Bendo et al. 2006). Analysis of the MIR emission from the First Look Survey (Fang et al. 2004) galaxies shows that the correlation between the *Spitzer* 8 μm band emission and tracers of the ionizing photons is shallower than unity (Wu et al. 2005), in agreement with the correlations observed for H II regions in the nearby, metal-rich, star-forming galaxy NGC 5194 (M51a; Calzetti et al. 2005).

The 24 μm emission is a close tracer of SFR in the dusty center of NGC 5194 (Calzetti et al. 2005) and in NGC 3031 (Perez-Gonzalez et al. 2006). The general applicability of this monochromatic indicator has so far been explored only for a small number of cases, mostly bright galaxies (e.g., Wu et al. 2005; Alonso-Herrero et al. 2006). A potential complication is that most of the energy from dust emerges at wavelengths longer than $\sim$40–50 μm (see Dale et al. 2007 and references therein). Thus, the MIR does not trace the bulk of the dust emission and, because it lies on the Wien side of the blackbody spectrum, could be sensitive to the dust temperature rather than linearly correlating with source luminosity.

This study investigates the use of the *Spitzer* IRAC 8 μm and MIPS 24 μm monochromatic luminosities as SFR indicators for star-forming regions in a subsample of the SINGS galaxies (SINGS, or the *Spitzer* Infrared Nearby Galaxies Survey, is one of the *Spitzer* Legacy Programs; Kennicutt et al. 2003). Star-forming regions in galaxies represent a first stepping stone for characterizing SFR indicators, as they can be considered simpler entities than entire galaxies.

We also extend our analysis to include both new and published integrated (galaxy wide) data on local low-metallicity starburst galaxies (Engelbracht et al. 2005) and luminous infrared galaxies (LIRGs; Alonso-Herrero et al. 2006). These data are used to explore whether the relationships derived for the star-forming regions that constitute our main sample are applicable to starburst-dominated galaxies as a whole. A future paper will investigate the viability of the MIR luminosities as SFR tracers for more general classes of galaxies (R. C. Kennicutt, Jr. & J. Moustakas 2007, in preparation).

The *Spitzer* observations are coupled with near-infrared *HST* NICMOS observations centered on the Paα hydrogen emission line (at 1.8756 μm) and with ground-based Hα observations obtained by the SINGS project. The hydrogen emission lines trace the number of ionizing photons, and the Paα line is only modestly impacted by dust extinction. Furthermore, the Paα and Hα lines are sufficiently separated in wavelength that reliable extinction corrections can be measured (Quillen & Yukita 2001). Because of its relative insensitivity to dust extinction (less than a factor of 2 correction for the typical extinction in our galaxies, $A_V \lesssim 5$ mag), Paα represents a nearly unbiased tracer of the current SFR over a timescale of about 10 Myr (Kennicutt 1998b). The access to Paα images to use as a yardstick for calibrating the MIR emission is the basic motivation for the present work.

The present paper is organized as follows. In § 2 we introduce the sample of local star-forming galaxies from SINGS, in § 3 we present the data, while the measurements used in the analysis are presented in § 4. Section 5 briefly introduces the low-metallicity starburst galaxies from Engelbracht et al. (2005) and the LIRGs from Alonso-Herrero et al. (2006). The main findings are reported in § 6, and the comparison with models is made in § 7. Discussion and a summary are given in §§ 8 and 9, respectively.

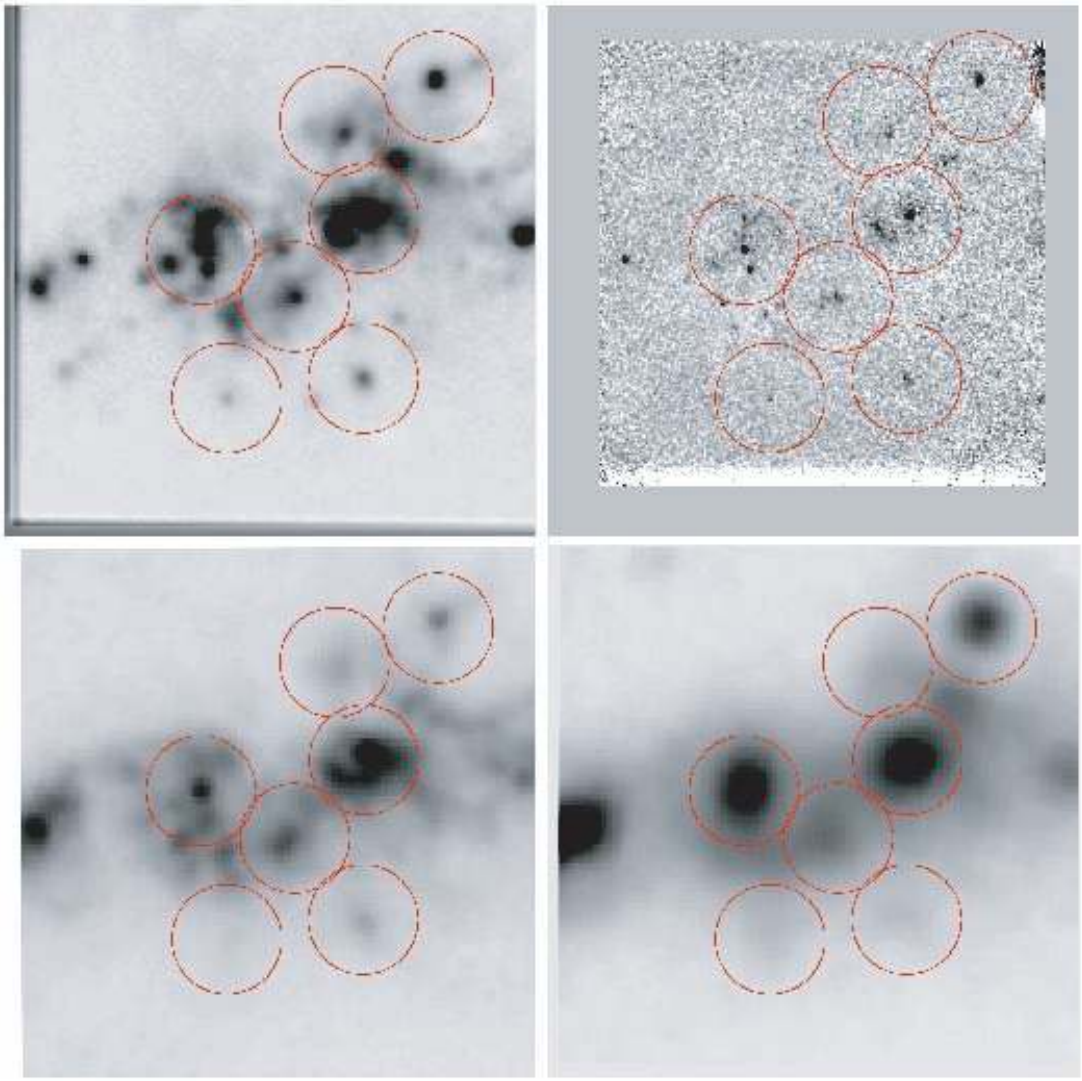

FIG. 1.—Example of aperture selection in one of our fields. The central $\sim 1'$ of the galaxy NGC 0925 is shown at Hα (*top left*), Paα (*top right*), stellar continuum–subtracted 8 μm (*bottom left*), and 24 μm (*bottom right*). The $13''$ apertures used for photometric measurements are shown as red circles and correspond to physical sizes of $\sim$580 pc. The field shown is one of the two obtained in the central region of this galaxy. North is up, and east is to the left.

Details on the models of dust absorption and emission are in the Appendix.

2. MAIN SAMPLE DESCRIPTION

The SINGS sample of 75 galaxies (Kennicutt et al. 2003) was used as our baseline sample for which *HST* observations in the infrared were either obtained as part of our project or retrieved from the *HST* archive (see details in § 3.2). The only criterion required for a SINGS galaxy to be observed with the *HST* was to have a redshifted Paα emission within the transmission curve of one of the NICMOS narrowband filters. A total of 39 galaxies, or 52% of the SINGS sample, were observed in the Paα line (example in Fig. 1). The *HST* NICMOS–observed galaxies are fully representative of the SINGS sample as a whole, in terms of morphological types, range of metallicity, and SFRs.

The infrared data of 4 of the 39 galaxies show nonrecoverable problems (see § 3.2 for additional explanation); two more galaxies, M81 dwA and DDO 154, do not show either optical line emission or MIR dust emission in the region imaged in the near-infrared with *HST*. All six galaxies were discarded from the current analysis, thus leaving a net sample of 33 galaxies. Table 1 lists the main characteristics of the 39 galaxies, separating the discarded ones from the remainder of the sample.

The 33 galaxies are divided into three groups according to their oxygen abundance: high-metallicity galaxies [$12 + \log(\mathrm{O/H}) > 8.35$], intermediate-metallicity galaxies [$8.00 < 12 + \log(\mathrm{O/H}) \lesssim 8.35$], and low-metallicity galaxies [$12 + \log(\mathrm{O/H}) \lesssim 8.00$]. The two sets of disk-averaged oxygen abundance values listed in Table 1 differ systematically by about 0.6 dex (J. Moustakas et al. 2007, in preparation). As described by J. Moustakas et al. (2007, in preparation), the set of lower numbers for the oxygen abundance is roughly tied to the electron temperature abundance scale (Pilyugin & Thuan 2005), while the higher abundance set is based on stellar populations plus photoionization modeling (Kobulnicky & Kewley 2004; Kewley & Dopita 2002). The difference between the two scales is due to an as yet unidentified systematic zero-point offset, and the "true" oxygen abundance should lie somewhere between the two listed values; however, the relative ranking of abundances on either of the scales should be fairly accurate. On this basis, we assign a galaxy to a metallicity bin based on the average of the two values. Metallicity gradients across galaxies are likely of little impact in our analysis.

TABLE 1
CHARACTERISTICS OF THE SAMPLE GALAXIES

Name	Morphology[a]	Nucleus[a]	v_H[a] (km s^{-1})	$E(B-V)_G$[a]	Distance[b] (Mpc)	M_V[c]	$12+\log(\mathrm{O/H})$[d]	Number of Regions[e]	*HST* ID[f]
High-Metallicity Galaxies									
NGC 0925	SAB(s)d	...	553	0.081	9.12	−20.33	8.24–8.78	10	7919, 9360
NGC 1512	SB(r)ab	...	898	0.011	10.5	−19.90	8.37–9.05	3	9360
NGC 2403	SAB(s)cd	...	131	0.043	3.5	−19.68	8.31–8.81	8	7919
NGC 2841	SA(r)b	Sy1/LIN	638	0.017	9.8	−21.12	8.52–9.19	5	7919
NGC 2976	SAc	...	3	0.074	3.5	−17.97	8.30–8.98	8	7919
NGC 3184	SAB(rs)cd	...	592	0.018	11.10	−20.46	8.48–9.14	6	9360
NGC 3198	SB(rs)c	...	663	0.013	13.68	−20.90	8.32–8.87	9	9360
NGC 3351	SB(r)b	...	778	0.030	10.1	−20.48	8.60–9.22	2	9360
NGC 3627	SAB(s)b	Sy2/LIN	727	0.035	8.7	−21.17	8.49–9.10	6	7919
NGC 3938	SA(s)c	...	809	0.023	12.2	−20.10	8.35–9.07	9	9360
NGC 4125	E6	LIN	1356	0.020	21.4	−21.89	8.58–9.21	1	9360
NGC 4559	SAB(rs)cd	...	816	0.019	11.1	−20.84	8.25–8.79	6	7919
NGC 4569	SAB(rs)ab	Sy/LIN	−235	0.049	16.58	−21.90	8.56–9.19	5	9360
NGC 4625	SAB(rs)m	...	609	0.019	9.17	−17.53	8.27–9.04	6	9360
NGC 4736	(R)SA(r)ab	Sy2	308	0.019	5.3	−20.59	8.31–9.01	5	9360
NGC 4826	(R)SA(rs)ab	Sy2	408	0.044	5.6	−20.63	8.59–9.24	8	9360
NGC 5033	SA(s)c	Sy1.9	875	0.012	13.28	−20.87	8.27–8.90	9	9360
NGC 5055	SA(rs)bc	LIN	504	0.019	7.82	−21.08	8.42–9.13	9	9360
NGC 5194	SA(s)bc	Sy2.5	463	0.037	8.2	−21.43	8.54–9.18	43	7237
NGC 5195	SB0_1	LIN	465	0.038	8.2	−19.99	8.28–8.83	1	9360
NGC 5866	S0_3	LIN	672	0.014	12.1	−20.52	8.43–9.02	3	9360
NGC 6946	SAB(rs)cd	...	48	0.365	5.0	−21.11	8.40–9.04	9	9360
NGC 7331	SA(s)b	LIN	816	0.097	15.1	−22.14	8.40–9.05	8	9360
Intermediate-Metallicity Galaxies									
NGC 1705	SA0−	...	632	0.009	5.1	−16.29	8.20–8.43	3	7919
IC 2574	SAB(s)m	...	57	0.039	2.8	−17.33	7.94–8.26	6	9360
NGC 4236	SB(s)dm	...	0	0.015	4.45	−19.12	8.07–8.56	3	9360
IC 4710	SB(s)m	...	739	0.095	7.8	−17.96	8.11–8.62	7	7919
NGC 6822	IB(s)m	...	−57	0.253	0.47	−14.97	8.04–8.67	3	7919
Low-Metallicity Galaxies									
Ho II	Im	...	142	0.035	3.5	−17.25	7.68–8.07	3	9360
DDO 053	Im	...	20	0.040	3.56	−13.68	7.77–8.13	6	9360
Ho IX	Im	...	46	0.085	3.3	−13.67	7.61–7.98	3	9360
M81 dwB	Im	...	347	0.085	6.5	−14.20	7.85–8.20	4	9360
NGC 5408	IB(s)m	...	506	0.074	4.8	−17.22	7.81–8.23	3	9360
Discarded Galaxies									
NGC 0024	SA(s)c	...	554	0.021	8.8	−19.01	8.32–8.92	...	9360
NGC 1291	(R_1)SB(1)0/a	...	839	0.014	10.5	−21.69	8.42–9.01	...	9360
M81 dwA	I?	...	113	0.022	3.55	...	7.34–7.64	...	9360
NGC 3034	I0	...	203	0.170	5.2	−20.51	8.36–9.09	...	7919
NGC 4631	SB(s)d	...	606	0.018	8.5	−21.59	8.13–8.76	...	9360
DDO 154	IB(s)m	...	374	0.010	4.3	−14.73	7.54–8.02	...	9360

[a] Galaxy morphologies, nuclear activity, heliocentric velocity, and foreground Galactic color excess are from the NASA/IPAC Extragalactic Database (NED). The nuclear activity is reported for those cases where nonthermal emission dominates the emission in the central region. The Galactic color excesses, $E(B-V)_G$, are from Schlegel et al. (1998).

[b] Adopted distances as derived by Masters (2005). Note that changes in the galaxy distances do not affect the analysis, which is based on LSDs (luminosity/area).

[c] Galaxy's absolute magnitude, based on V_T^0 from the RC3 (de Vaucouleurs et al. 1991), as retrieved from NED. For NGC 6822 the B_T^0 and for M81 dwB the m_B^0 values have been used.

[d] Oxygen abundances; the two columns of values are from J. Moustakas et al. (2007, in preparation); see § 2 for a brief description of their derivation.

[e] Number of independent regions measured in the galaxy.

[f] *HST* program ID for the NICMOS observations used in this paper.

The observations probe the inner ≈0.8–5.1 kpc, depending on the distance; typical metallicity variations over these region sizes are less than ∼0.3 dex for our spiral galaxies (J. Moustakas et al. 2007, in preparation) and therefore are not expected to play a significant role in our results.

Within the area imaged by the *HST* NICMOS for each galaxy in the main sample (Table 1), regions of star formation are identified and their fluxes measured over typical sizes of ∼200–600 pc (§ 4 and Fig. 1). These regions are termed here "H II knots," and they are far simpler units, in terms of stellar population and

star formation history, than whole galaxies. The H II knots in this study cannot be considered individual H II regions in the strict meaning of the term. Limitations in angular resolution, as discussed in § 4, force us to consider areas within galaxies that may be populated by multiple H II regions. The main requirement is for such areas to be local peaks of *current* star formation, as determined from hydrogen line or infrared emission. The ionizing populations in these regions can be approximated as having comparable ages, and more evolved stellar populations do not tend to dominate the radiation output. Although caution should be used when deriving an SFR for quasi-single-age populations, the investigation of simpler, star formation–dominated structures should offer better insights than whole galaxies on the strengths and weaknesses of the MIR SFR indicators of interest here.

Details on the low-metallicity starburst galaxies from Engelbracht et al. (2005) and on the LIRGs from Alonso-Herrero et al. (2006) are given in § 5.

3. OBSERVATIONS AND DATA REDUCTION

3.1. *Spitzer IRAC and MIPS Imaging Data*

Spitzer images for the galaxies in Table 1 were obtained with both IRAC (3.6, 4.5, 5.8, and 8.0 μm) and MIPS (24, 70, and 160 μm), as part of the SINGS Legacy project, between ~2004 March and ~2005 August. A description of this project and the observing strategy can be found in Kennicutt et al. (2003).

Each galaxy was observed twice in each of the four IRAC bands, with a grid covering the entire galaxy and the surrounding sky. The observing strategy allowed a separation of a few days between the two observations to enable recognition and exclusion of asteroids and detector artifacts. Total exposure times in each filter are 240 s in the center of the field and 120 s along the grids' edges. The SINGS IRAC pipeline was used to create the final mosaics, which exploits the subpixel dithering to better sample the emission and resamples each mosaic into 0.75″ pixels (Regan et al. 2004). The measured 8 μm point-spread function (PSF) FWHM is, on average, 1.9″, and the 1 σ sensitivity limit in the central portion of the 8 μm mosaic is 1.2×10^{-6} Jy arcsec^{-2}.

As the interest in this paper is in using the dust emission at MIR wavelengths (8 and 24 μm) as SFR tracers, we need to remove the stellar continuum contribution from the 8 μm images. This contribution is, in general, small in high-metallicity, dusty galaxies (e.g., Calzetti et al. 2005) but can become significant in lower metallicity and more dust-poor galaxies. "Dust emission" images at 8 μm are obtained by subtracting the stellar contribution using the recipe of Helou et al. (2004):

$$f_{8\ \mu\mathrm{m,\,dust}}(\nu) = f_{8\ \mu\mathrm{m}}(\nu) - \beta f_{3.6\ \mu\mathrm{m}}(\nu), \quad (1)$$

where the coefficient β is in the range 0.22–0.29, as determined from isolated stars in the galaxies' fields. Visual inspection of the stellar continuum–subtracted images suggests that this approach is fairly accurate in removing stellar emission; occasional foreground stars located along the galaxies' lines of sight are in general removed by this technique. Although the 3.6 μm images can include, in addition to photospheric emission from stars, a component of hot dust emission, this component is unlikely to have an impact beyond a few percent on the photometry of the dust-only 8 μm images (Calzetti et al. 2005).

MIPS observations of the galaxies were obtained as scan maps, with enough coverage to include surrounding background in addition to the galaxy. The reduction steps for MIPS mosaics are described in Gordon et al. (2005) and Bendo et al. (2006). At 24 μm, the PSF FWHM is ~5.7″, and the 1 σ detection limit is 1.1×10^{-6} Jy arcsec^{-2}. The MIPS images are considered "dust" images for all purposes, as contributions from the photospheric emission of stars and from nebular emission are negligible (a few percent) at these wavelengths.

3.2. *HST Imaging Data*

The main advantage of using near-infrared narrowband imaging, rather than spectroscopy, is the potential of capturing, in principle, all of the light in the Paα line, thus enabling a more secure measurement of the total line emission from the targets. The *HST* NICMOS narrowband filters of interest here have ~1% bandpasses, which can easily accommodate gas line emission with a few hundred kilometer per second shift relative to the galaxy's systemic velocity.

Most of the *HST* NICMOS observations for the galaxies in our sample come from the *HST* SNAP program 9360 (PI: Kennicutt). For nine of the galaxies, archival *HST* data were used, from programs GO-7237 and SNAP-7919.

Observations for SNAP-9360 were obtained with the NIC3 camera, in the narrowband filters F187N and F190N (Paα emission line at rest-frame wavelength $\lambda = 1.8756$ μm and adjacent stellar continuum) and the broadband filter F160W. The NIC3 camera has a field of view (FOV) of 51″, and observations were obtained with four dithered pointings along a square pattern with 0.9″ sides, to better remove cosmic rays and bad pixels. Thus, NICMOS observations imaged the central $\lesssim$1′ of each galaxy. The NIC3 0.2″ pixels undersample the NICMOS PSF, although this is not a concern for the diffuse ionized gas emission. On-target total exposure times were 640, 768, and 96 s for F187N, F190N, and F160W, respectively.

The data were reduced with the STScI IRAF/STSDAS pipeline `calnica`, which removes instrumental effects, bad pixels, and cosmic rays and produces images in count rate units. The removal of the quadrant-dependent "pedestal" was done with the IRAF/STSDAS routine `pedsub`. The four dithered exposures were combined with the IRAF/STSDAS mosaicking pipeline `calnicb`.

For our analysis, only the two narrowband images are used, and the emission-line-only images are obtained by subtracting the continuum-only images, rescaled by the ratio of the filters' efficiencies, from the line+continuum image. Program 9360 was executed after the NICMOS Cryocooler System (NCS) had been installed on the *HST*, providing a detector quantum efficiency about 30% higher in the *H* band than during pre-NCS (i.e., pre-2002) operations (Barker et al. 2006[17]). This is an important difference when comparing depths of SNAP-9360 with those of the archival NICMOS images, which were obtained pre-NCS. The average 1 σ sensitivity limit of the continuum-subtracted image is 6.4×10^{-17} ergs s^{-1} cm^{-2} arcsec^{-2}. In units that will be easier to relate to the analysis performed in this paper, our 1 σ limit for a specific Paα luminosity measured in a 13″ diameter aperture is 2.83×10^{37} ergs s^{-1} kpc^{-2}; in a 50″ diameter aperture, the 1 σ limit is 1.04×10^{38} ergs s^{-1} kpc^{-2}.

The archival NICMOS data from *HST* snapshot program 7919 are described in Böker et al. (1999). Here we summarize the main differences with SNAP-9360. Data for SNAP-7919 were obtained with a single pointing (and a single integration) of the galaxy's center with the NIC3 camera. One narrowband filter (F187N or F190N depending on redshift) and the broadband F160W filter were used, for ~768 and 192 s, respectively. We reprocessed the archival images through `calnica`, to improve the removal of instrumental effects and of cosmic rays by using a more

[17] See http://www.stsci.edu/hst/nicmos/documents/handbooks/handbooks/current_NEW/nicmos_ihb.pdf.

recent version of the calibration pipeline than the one used in Böker et al. (1999); the quadrant-dependent pedestal was removed with `pedsub`. As in Böker et al. (1999), the rescaled broadband filter is used for removal of the underlying stellar continuum from the image containing the Paα emission line. The images from SNAP-7919 are deeper than in SNAP-9360, with an average 1 σ sensitivity limit of the continuum-subtracted image of 3.5×10^{-17} ergs s^{-1} cm^{-2} arcsec^{-2}.

Broadband filters may not provide the optimal underlying stellar continuum signature, especially if uneven dust extinction in the galaxy produces color variations within the filter's bandpass. To check the impact of this potential effect, we have compared observations of galaxies in common between the SNAP-9360 and SNAP-7919 programs: NGC 3184, NGC 4826, NGC 5055, and NGC 6946 (images of NGC 0925 are also present in both programs, but the pointings are only partially overlapping and are sufficiently different that both images are used in our analysis; see Table 1). For SNAP-9360, two narrowband images are available, thus yielding a "cleaner" line image. Comparison of continuum-subtracted images in both programs for regions in the common galaxies yields differences in the Paα photometry in the range 10%–30%, which is in general well within our random uncertainty for the Paα measurements (§ 4.2).

The NICMOS archival data for NGC 5194 (*HST* program 7237) are described in Scoville et al. (2001) and Calzetti et al. (2005). The main difference with the data in SNAP-9360 is that the NGC 5194 image is a 3×3 NIC3 mosaic that spans the central 144 arcsec^2. Each pointing was observed in both F187N and F190N, with 128 s exposure times. The sensitivity is variable, being lower at the seams of the nine images that form the mosaic. The average 1 σ sensitivity limit of the continuum-subtracted image for this galaxy is 1.8×10^{-16} ergs s^{-1} cm^{-2} arcsec^{-2}.

The *HST* NICMOS observations are the shallowest in our sample when compared to the other images and represent the true limitation to our analysis. On the other hand, Paα measurements offer an opportunity to obtain a nearly unbiased measure of the number of ionizing photons produced in a region, as it is only weakly affected by dust extinction. An extinction as large as 5 mag at V produces an extinction of 0.73 mag at Paα, i.e., roughly a change of a factor of 2 in the line intensity (Fig. 2), for foreground screen dust geometry. Still, we combine the Paα measurements with complementary measurements at Hα to correct the line emission for the effects of dust. We adopt a metallicity-dependent intrinsic ratio Hα/Paα = 7.82, 8.45, and 8.73 for the high-, intermediate-, and low-metallicity subsamples, respectively, which correspond to electron temperatures T_e = 7000, 10,000, and 12,500 K for the H II knots (for n_e = 100 cm^{-3}; Osterbrock & Ferland 2006; Garnett et al. 2004). We also adopt an extinction curve[18] with differential value $k(\mathrm{H}\alpha) - k(\mathrm{Pa}\alpha) = 2.08$ (Fitzpatrick 1986; Landini et al. 1984).

Four of the galaxies discarded from our sample (Table 1) present an array of problems mainly in their NICMOS observations. The F187N image of NGC 0024 is heavily affected by cosmic-ray persistence, which has caused the effective noise level of the frame to be about 7 times higher than nominal; the net result is that the faint emission from the galaxy is undetectable. The NICMOS frames of NGC 1291 missed the galaxy because of guide star problems. The F187N images of NGC 4631 show a faint flat-field imprint (generally a sign of residual pedestal) that, coupled with the large dynamical range of the emission from this edge-on galaxy, produces a very uneven background. For NGC 3034 (M82), problems related to nonlinearity corrections and saturation for this bright target exist for the NICMOS, IRAC, and MIPS images, making photometry in the center of this object highly unreliable at the present time.

[18] The extinction curve $k(\lambda)$ is defined through the following equation: $F_{\mathrm{obs}}(\lambda) = F_{\mathrm{int}}(\lambda) 10^{-0.4k(\lambda)E(B-V)}$, where F_{obs} and F_{int} are the observed and intrinsic fluxes, respectively, and $E(B-V)$ is the color excess.

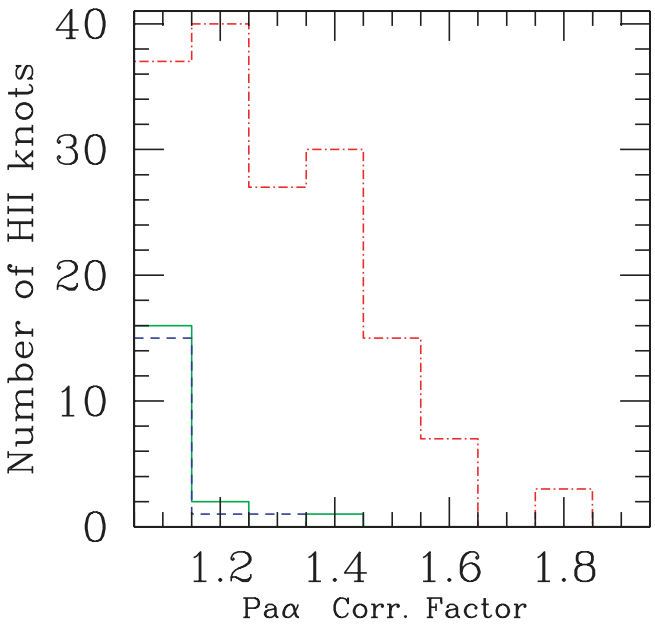

FIG. 2.—Histogram of the multiplicative factors applied to the observed Paα line emission to correct for the effects of dust extinction, as determined using the Hα/Paα ratio (§ 3.2). The vertical axis shows the number of H II knots to which each correction factor is applied. The high- [$12 + \log(\mathrm{O/H}) > 8.35$], intermediate- [$8.00 < 12 + \log(\mathrm{O/H}) \lesssim 8.35$], and low-metallicity [$12 + \log(\mathrm{O/H}) \lesssim 8.00$] regions (§ 2) are shown as three separate histograms, coded as a red dot-dashed line, green solid line, and blue dashed line, respectively. Most corrections are less than 50%.

The *HST* archive was also mined for Hα images for those cases where (1) coverage was similar between NIC3 and optical images and (2) the narrowband filter provides a better rejection of the [N II] emission line than the ground-based images. WFPC2 images that met these criteria were available for NGC 1512, NGC 4736, NGC 4826, and NGC 5055. The line emission was observed through the narrowband filters F656N or F658N, and the underlying continuum through F547M, F555W, and/or F814W (equivalent to medium-*V*, *V*, and *I*, respectively). For NGC 4736, NGC 4826, and NGC 5055, the [N II]/Hα values listed in Table 2 come from the comparison of the fluxes in the *HST* and ground-based (see below) narrowband filters; the [N II] contamination in the *HST* filters is minimal and has been used to guide our extrapolation of the best nitrogen-to-Hα ratio to attribute to each galaxy. This value has been used for those areas in the ground-based images not covered by the *HST*.

3.3. *Ground-based Optical Imaging Data*

R-band and Hα-centered narrowband images were obtained for most of the galaxies as part of the SINGS ancillary data program, either at the 2.1 m Kitt Peak National Observatory (KPNO) telescope or at the 1.5 m Cerro Tololo Inter-American Observatory (CTIO) telescope (Kennicutt et al. 2003). Exposure times were typically around 1800 s for the narrowband filters and a few hundred seconds for *R*. Standard reduction procedures were applied to all the images. Standard-star observations were obtained during each observing run to derive photometric calibrations.

TABLE 2
GALACTIC MEASUREMENTS

Name	$\log S_{Pa\alpha,corr}$[a] (ergs s^{-1} kpc^{-2})	$\log S_{H\alpha,obs}$[a] (ergs s^{-1} kpc^{-2})	[N II]/Hα[b]	A_V[a] (mag)	$\log S_{8\,\mu m,dust}$[a] (ergs s^{-1} kpc^{-2})	$\log S_{24\,\mu m}$[a] (ergs s^{-1} kpc^{-2})
High-Metallicity Galaxies						
NGC 0925	38.44 ± 0.18	39.18 ± 0.08	0.24	0.45 ± 0.19	41.02 ± 0.11	40.48 ± 0.11
NGC 1512	38.55 ± 0.06	38.80 ± 0.02	0.47	1.94 ± 0.06	41.09 ± 0.06	40.75 ± 0.06
NGC 2403	38.73 ± 0.15	39.27 ± 0.08	0.62	1.07 ± 0.17	41.24 ± 0.11	40.35 ± 0.11
NGC 2841	37.83 ± 0.30	38.03 ± 0.30	0.55A	2.12 ± 0.43	40.43 ± 0.08	40.08 ± 0.08
NGC 2976	38.50 ± 0.15	39.12 ± 0.08	0.30	0.83 ± 0.17	41.12 ± 0.10	40.59 ± 0.10
NGC 3184	38.59 ± 0.18	38.72 ± 0.11	0.44	2.31 ± 0.21	40.97 ± 0.11	40.69 ± 0.11
NGC 3198	38.56 ± 0.18	38.42 ± 0.08	0.36	3.16 ± 0.19	41.20 ± 0.10	41.09 ± 0.10
NGC 3351	39.24 ± 0.06	39.48 ± 0.04	0.40	1.97 ± 0.07	41.72 ± 0.06	41.68 ± 0.06
NGC 3627	38.92 ± 0.23	39.18 ± 0.04	0.55A	1.94 ± 0.23	41.72 ± 0.11	41.33 ± 0.11
NGC 3938	37.99 ± 0.30	38.76 ± 0.06	0.54	0.38 ± 0.31	41.08 ± 0.08	40.46 ± 0.08
NGC 4125[c]	37.13U	36.00U	...	...	40.15 ± 0.06	39.95 ± 0.06
NGC 4559	38.51 ± 0.30	39.33 ± 0.08	0.32	0.24 ± 0.31	41.30 ± 0.08	40.75 ± 0.08
NGC 4569	38.29 ± 0.30	38.84 ± 0.04	0.50A	1.05 ± 0.30	41.56 ± 0.08	41.35 ± 0.08
NGC 4625	38.06 ± 0.11	38.95 ± 0.08	0.46	0.03 ± 0.14	40.79 ± 0.08	40.39 ± 0.07
NGC 4736	37.96 ± 0.18	38.88 ± 0.04	0.50[d]	0.01 ± 0.18	41.96 ± 0.08	41.54 ± 0.08
NGC 4826	39.28 ± 0.06	39.53 ± 0.02	0.55[d]	1.97 ± 0.06	42.12 ± 0.06	41.69 ± 0.06
NGC 5033[e]	38.57 ± 0.08...	...	...	41.88 ± 0.06	41.35 ± 0.06	...
NGC 5055	38.61 ± 0.11	39.28 ± 0.08	0.50[d]	0.68 ± 0.14	41.74 ± 0.06	41.17 ± 0.06
NGC 5194	38.95 ± 0.06	39.26 ± 0.04	0.50	1.78 ± 0.07	41.54 ± 0.06	41.19 ± 0.06
NGC 5195[c]	36.89U	37.83U	...	...	42.39 ± 0.06	41.35 ± 0.06
NGC 5866	37.64 ± 0.30	38.19 ± 0.11	0.55A	1.04 ± 0.32	40.04 ± 0.06	39.47 ± 0.06
NGC 6946	39.44 ± 0.06	39.77 ± 0.04	0.56	1.72 ± 0.07	42.34 ± 0.06	42.20 ± 0.06
NGC 7331	39.08 ± 0.11	39.14 ± 0.08	0.32	2.54 ± 0.14	41.69 ± 0.08	41.20 ± 0.08
Intermediate-Metallicity Galaxies						
NGC 1705	38.56 ± 0.11	39.48 ± 0.11	0.09	0.03 ± 0.16	40.09 ± 0.06	40.06 ± 0.06
IC 2574	37.55 ± 0.30	38.44 ± 0.08	0.12	0.14 ± 0.31	39.17 ± 0.18	39.18 ± 0.18
NGC 4236	37.57 ± 0.30	38.15 ± 0.08	0.17[f]	1.09 ± 0.31	39.76 ± 0.18	39.42 ± 0.18
IC 4710	37.81 ± 0.30	38.56 ± 0.08	[g]	0.57 ± 0.31	39.64 ± 0.11	39.10 ± 0.11
NGC 6822	37.85 ± 0.30	38.74 ± 0.11	[g]	0.12 ± 0.32	39.46 ± 0.30	39.13 ± 0.30
Low-Metallicity Galaxies						
Ho II	38.37 ± 0.30	39.31 ± 0.04	0.10A	0.01 ± 0.30	40.01 ± 0.13	40.06 ± 0.13
DDO 053	37.97 ± 0.30	38.91 ± 0.11	0.04	0.01 ± 0.32	39.33 ± 0.18	39.82 ± 0.18
Ho IX[h]	36.12 ± 0.73	36.32 ± 0.2	0.05A	...	36.92U	38.14 ± 0.30
M81 dwB	37.76 ± 0.18	38.60 ± 0.08	0.04	0.29 ± 0.19	39.03 ± 0.11	39.15 ± 0.11
NGC 5408	38.26 ± 0.30	39.20 ± 0.04	0.02[f]	0.01 ± 0.30	39.29 ± 0.06	40.05 ± 0.06

[a] Average LSD and extinction in the central $\sim 50'' \times 50''$ of each galaxy ($\sim 144'' \times 144''$ for NGC 5194). The extinction-corrected and the "observed" (not extinction corrected) values are listed for Paα and Hα, respectively.

[b] [N II] λ6584/Hα, as obtained from spectroscopy (J. Moustakas et al. 2007, in preparation), and before convolution with the narrowband filters' transmission curves. An "A" after a value indicates an adopted (nonmeasured) value, for those cases where a spectrum is not available or the available spectrum is dominated by a central nonthermal source. Adopted values come from galaxies of comparable metallicity to the target ones.

[c] For NGC 4125 and NGC 5195, the only detected sources are the central Sy2 nuclei; for these, only 8 and 24 μm emission is detected, while Hα and Paα are upper limits.

[d] For NGC 4736, NGC 4826, and NGC 5055, the [N II]/Hα values are derived from the comparison of the *HST* and ground-based narrowband images. The *HST* narrowband filters centered on Hα reject almost completely [N II], thus providing a reference for the ground-based images.

[e] For NGC 5033, no Hα data are available.

[f] Values from the spectrum of Ho et al. (1997) (NGC 4236) and Masegosa et al. (1994) (NGC 5408).

[g] For IC 4710 and NGC 6822, no ratios are available. However, the [N II] contribution to the narrowband Hα filter is negligible for these two galaxies, since both galaxies have low metallicity and the narrowband filters transmit less than 3% and 4% of the light from the [N II] $\lambda\lambda$6548 and 6584 lines, respectively.

[h] The Paα emission for Ho IX is the middle value between the upper limit measured from the *HST* NICMOS image and the lower limit represented by the detected Hα emission at zero extinction (§ 4.2); the emission at 8 μm for the galaxy is an upper limit.

The rescaled broadband images were subtracted from the narrowband images to obtain emission-line-only images. The [N II] contamination within the filter bandpass is removed using [N II]/Hα values either measured from large-aperture ($\approx 50''$) SINGS optical spectroscopy (J. Moustakas et al. 2007, in preparation) or retrieved from the literature (Table 2), and accounting for changes in the filter transmission between the wavelengths of Hα and the two [N II] emission lines. High-metallicity galaxies for which [N II]/Hα ratios are not available from either source, or cases that have optical spectra dominated by a central nonthermal source (Seyfert 2 or LINER; J. Moustakas et al. 2007, in preparation), are assumed to have [N II]/H$\alpha \sim 0.5$. Within each galaxy, a constant [N II]/Hα is adopted, although the ratio can change significantly from individual H II regions to the more diffuse component (Hoopes & Walterbos 2003). Radial variations of [N II]/Hα within a galaxy are less of

a concern here, as only the central region of each galaxy is imaged.

Typical 1 σ sensitivity limits of the final Hα images are $(1–2)\times10^{-17}$ ergs s^{-1} cm^{-2} arcsec^{-2}; i.e., they are a factor of 3–10 deeper than the Paα images. This, coupled with the fact that the Hα is, intrinsically, about 8 times brighter than Paα, implies that our Hα measurements will have a higher signal-to-noise ratio than the Paα ones for $A_V \lesssim 4$ mag.

Narrowband and *R*-band images of DDO 053, M81 dwB, Holmberg 9, and NGC 4625 were obtained using a CCD imager on the Steward Observatory Bok 2.3 m telescope, as part of the 11HUGS project (R. C. Kennicutt, Jr. et al. 2007, in preparation). Narrowband and *R*-band images of NGC 5408 were obtained at the CTIO 0.9 m telescope, also as part of the 11HUGS project. Images were taken using a 70 Å narrowband filter centered at 6580 Å, and an *R*-band filter and a Loral 2k $\times$ 2k CCD detector. Exposure times were 1000 s in Hα and 200 s in *R* and reach comparable depth to the KPNO images because of the high throughputs of the filter and the CCD detector. Data reduction followed similar procedures as described above.

Ground-based Hα images for NGC 3627, NGC 4736, NGC 4826, and NGC 5055 were provided by the SONG collaboration (Sheth et al. 2002; Helfer et al. 2003), as SINGS did not repeat these observations. The data were obtained at the KPNO 0.9 m telescope, with an observing strategy and filter selection similar to those of SINGS. The main difference between the SINGS and SONG Hα images is the total exposure time (and the depth of the images), being in the latter case 3–5 times shorter than in the former. For this reason, the ground-based SONG images were used in conjunction with the *HST* Hα images for photometric measurements in NGC 4736, NGC 4826, and NGC 5055.

4. PHOTOMETRIC MEASUREMENTS

4.1. *Aperture Photometry*

For each galaxy, the Hα, stellar continuum–subtracted 8 μm, and 24 μm images were registered to the same coordinate system of the Paα image, before performing measurements. Photometric measurements at all four wavelengths of local 24 μm and Hα peaks were performed on the common FOV of the four images. Emission peaks at 24 μm (and 8 μm) have generally corresponding Hα peaks; the opposite, however, is not always true, and there are some cases of Hα emission peaks without corresponding MIR emission. Thus, both 24 μm and Hα images were used independently to locate local peaks of star formation.

The size of the aperture used for photometric measurements is dictated by the lowest angular resolution image, the MIPS 24 μm image, with a PSF FWHM $\sim 6''$. We chose apertures with $13''$ diameter as a compromise between the desire to sample the smallest possible scale compatible with H II regions and the necessity to have reasonable aperture corrections on the photometry (Fig. 1). For the chosen aperture size, corrections to infinite aperture are 1.045, 1.05, and 1.67 at 3.6, 8, and 24 μm, respectively, for point sources (SSC IRAC Handbook and MIPS Handbook, respectively; Reach et al. 2005; Engelbracht et al. 2007; Jarrett 2006[19]) and are assumed to be small or negligible in the Paα and Hα images (Calzetti et al. 2005).

In the case of the IRAC 3.6 and 8 μm emission, extended emission has an aperture correction different from the point sources. Best current estimates (Jarrett 2006) indicate that our aperture choice requires an additional correction factor of 1.02 at 3.6 μm and 0.90 at 8 μm, for extended sources. As our sources are neither totally extended nor pointlike, actual aperture corrections are likely to be closer to a value of unity than those reported here.

The fixed aperture corresponds to different spatial scales in different galaxies, as distances between $\sim$0.5 Mpc (spatial scale $\sim$30 pc) and $\sim$20 Mpc ($\sim$1.26 kpc) are covered. In order to allow comparison among luminosities measured over areas that differ by a factor of as much as $\sim$40 (for the typical distance range 3–20 Mpc), we report all measurements as luminosities per unit of physical area (luminosity surface density [LSD]) $S_{\mathrm{Pa}\alpha}$, $S_{\mathrm{H}\alpha}$, $S_{8\ \mu\mathrm{m,dust}}$, and $S_{24\ \mu\mathrm{m}}$, in units of ergs s^{-1} kpc^{-2}. Luminosities at MIR wavelengths are expressed as $\nu L(\nu)$.

The use of LSDs removes most dependence of our measurements with distance, as the LSDs are, for our purposes, equivalent to fluxes. Notable exceptions are the cases where the area covered by our aperture contains only one H II region, with intrinsic size smaller than our adopted fixed aperture's size; in these cases the LSDs will be artificially decreased by the larger area of the aperture relative to the values they would have if we selected apertures matched to the intrinsic size of each H II region/complex. The latter choice is not easily applicable to our sample due to the angular resolution limitations of some of the data. Furthermore, we see in § 6 that this effect does not appear to have an important impact on our results.

Photometry for a total of 220 separate H II knots is obtained in the 33 galaxies. Of these, 179 are in the 23 high-metallicity galaxies, including 11 nonthermal nuclei (Seyfert 2 or LINERs as retrieved from NED;[20] no aperture was laid on top of the active nucleus of the edge-on galaxy NGC 5866). In the five intermediate-metallicity and five low-metallicity galaxies, 22 and 19 regions are measured, respectively, including four regions (one each in IC 2574, Holmberg IX, M81 dwB, and NGC 6822) that are strongly emitting in the MIR but are undetected in both our Paα and Hα data. These line-undetected objects are detected in the optical continuum bands and are extended; thus, they are likely background sources. Heavily obscured sources, like those discussed in Prescott et al. (2007), should represent about 3% of the 24 μm sources, but we find none; we attribute this lack of heavily obscured sources in our sample to the small spatial region subtended by the NICMOS FOV within each galaxy. The 11 nonthermal sources and the four background sources (Figs. 3 and 4) will be excluded from all subsequent statistical analysis.

Crowding of emission peaks within each frame prevents the use of "annuli" around individual apertures to perform background subtraction from the photometric measurements. Background removal is thus achieved by subtracting a mode from each frame, as described in Calzetti et al. (2005).

"Integrated" values of Hα, Paα, 8 μm, and 24 μm LSD are also derived for each galaxy within the area imaged by the NICMOS NIC3 camera. These integrated values are therefore the LSD of each galaxy within the central $\sim 50''$, except for NGC 5194, where the central $\sim 144''$ are measured (Table 2). The integrated values mix the emission from the star-forming regions (measured with the smaller apertures) with areas of little or no star formation, thus providing some insights into the impact of the complex galactic environment on SFR calibrations.

[19] See http://ssc.spitzer.caltech.edu/irac/calib/extcal.

[20] The exact classification of galactic nuclei is beyond the scope of the present work; we restrict ourselves to well-known nonthermal sources as described in the literature, as these are the sources that deviate most from the general trends described in the following sections.

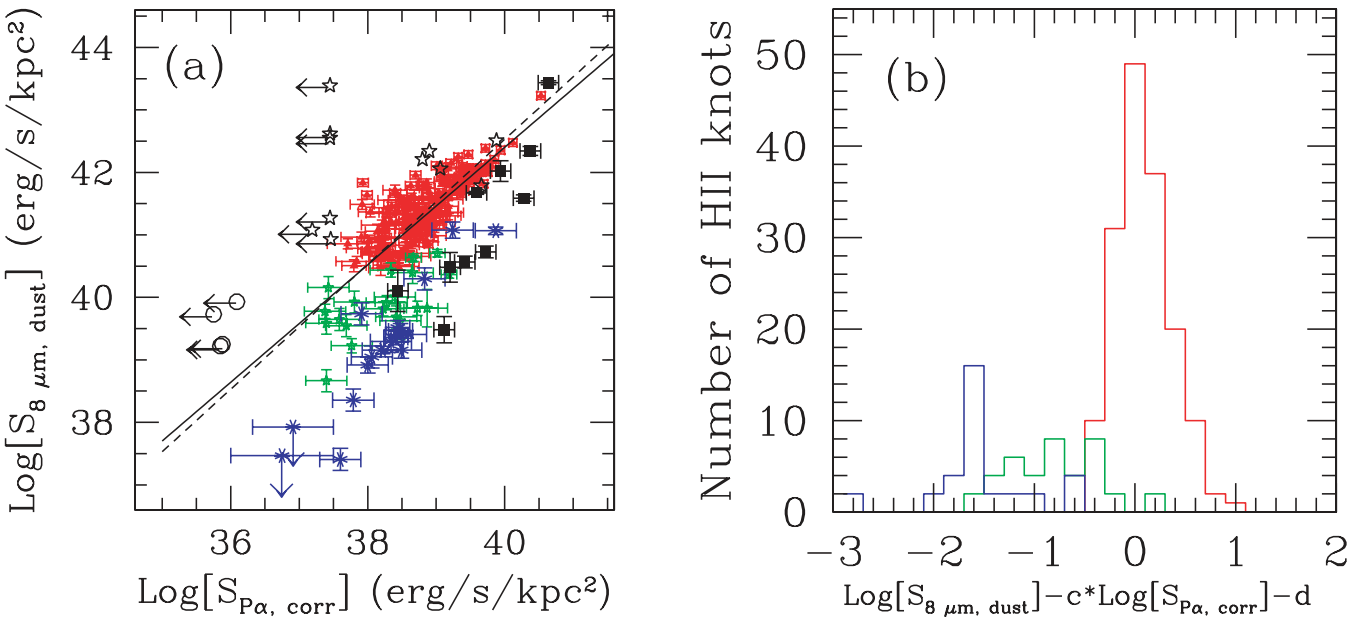

FIG. 3.—(*a*) LSD at 8 μm, $S_{8\ \mu m,dust}$, as a function of the extinction-corrected LSD at Paα, $S_{Pa\alpha,corr}$, for the 220 H II knots in the 33 galaxies for which photometric measurements have been obtained. LSDs are averaged over 13″ photometric apertures. The 8 μm emission is stellar continuum subtracted (§ 3.1). Data points are divided into three metallicity bins: high (*red filled triangles*), intermediate (*green stars*), and low (*blue asterisks*) oxygen abundance (§ 2). Filled black squares mark the local starbursts from the sample of Engelbracht et al. (2005) (§ 5.1). The 3 σ error bars are indicated for each data point. Open black stars indicate the location of the nonthermal sources (Seyfert 2s or LINERs; § 4.1), and open black circles indicate extended background sources. The best-fit line through the high-metallicity (*red*) data points is shown as a solid line, while the dashed line is the linear fit through the same data points with fixed slope of 1. (*b*) Histogram of the deviation of the H II knot data in panel *a* from the best-fit line through the high-metallicity data (the solid line in panel *a*). The values of the best-fit coefficients are $c = 0.94 \pm 0.02$ and $d = 4.80 \pm 0.85$ (eq. [2]). Three separate histograms are shown, for high- (*red*), intermediate- (*green*), and low-metallicity (*blue*) data. The intermediate- and low-metallicity histograms have been multiplied by a factor of 2 to make them visible.

4.2. *Uncertainties in the Photometric Measurements*

The uncertainties assigned to the photometric values at each wavelength and for each galaxy are the quadrature combination of four contributions: Poisson noise, variance of the background, photometric calibration uncertainties, and variations from potential misregistration of the multiwavelength images. The variance on the image background is derived in each case from the original-pixel-size images. The impact of potential background under- or oversubtractions varies from galaxy to galaxy and also depends on the relative brightness of the background and the sources. The effect of potential misregistrations has been evaluated

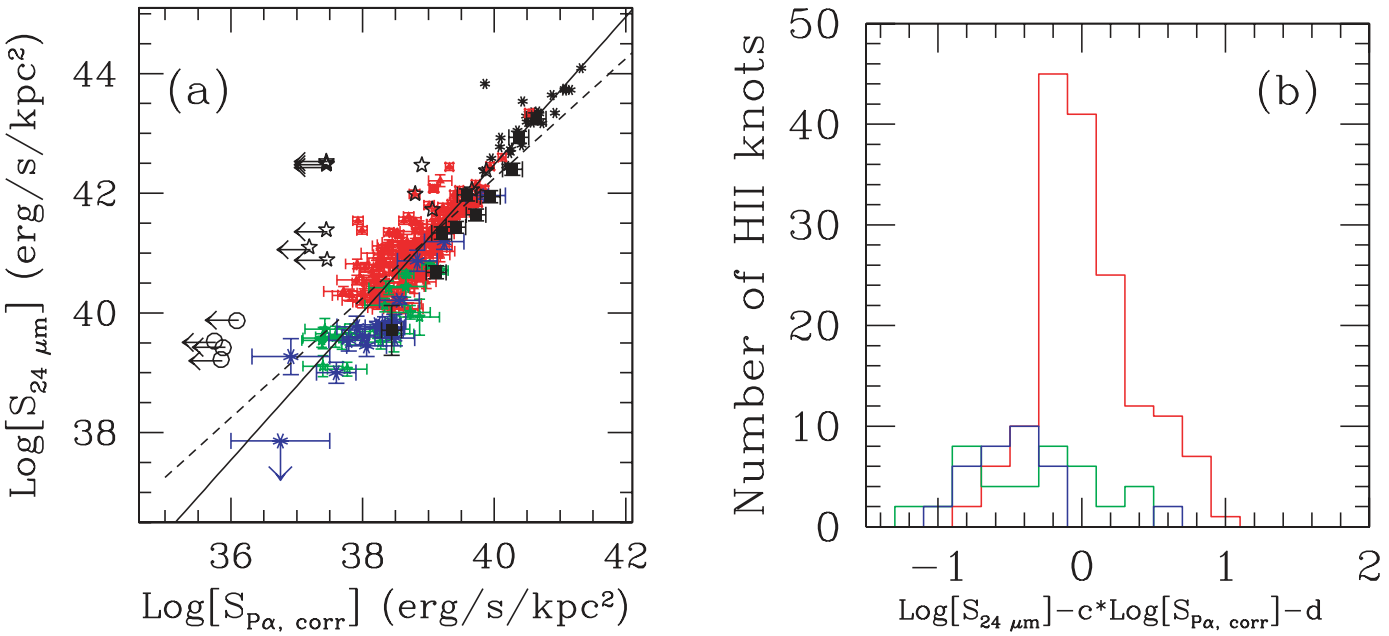

FIG. 4.—Same as Fig. 3, but for the LSD at 24 μm, $S_{24\ \mu m}$. In addition to the same data points as Fig. 3, panel *a* also reports the LIRGs from the sample of Alonso-Herrero et al. (2006) (*black asterisks*; § 5.2). The values of the parameters (*c, d*) in the horizontal axis of panel *b* are given in eq. (3) and are $c = 1.23 \pm 0.03$ and $d = -6.88 \pm 0.97$.

for the case of NGC 5194 by Calzetti et al. (2005). Because of the large apertures employed for our photometry, this contribution is either small (a few percent of the total uncertainty) or negligible.

For the *Spitzer* 8 and 24 μm images, calibration uncertainties are around 3% and 4%, respectively (Reach et al. 2005; Engelbracht et al. 2007). This, added in quadrature to the other uncertainties, produces overall uncertainties in the measurements that range between 15% and a factor of 2, with the median value being around 22%. The superposition of the PSF wings in adjacent apertures produces an additional effect in the 24 μm measurements, which is evaluated and removed on a case-by-case basis (see example in Calzetti et al. 2005).

For the *HST* images, photometric calibrations are generally accurate to within $\sim$5%, for narrowband filters. The faintness of the Paα emission, and therefore the impact of the background variance and stellar continuum subtraction, is what mostly dominates the photometric uncertainty on the Paα emission line measurements, with values between 15% and a factor of roughly 2, with a median value of 60%. For the extinction-corrected Paα luminosities, the uncertainty on the attenuation A_V increases the Paα uncertainty by a factor of 1.22.

For the ground-based Hα images, which are the deepest images in our set, the main sources of uncertainty are photometric calibrations, stellar continuum subtraction, and the correction for the [N II] contribution to the flux in the narrowband filter. These translate into uncertainties in the final photometric values between 10% and 50% (with occasional factor of 2 uncertainty). The median uncertainty for the Hα luminosities is 20%. Although less deep, the *HST* Hα images are characterized by more stable photometry, better continuum subtraction, and smaller [N II] contamination; uncertainties on the final luminosities are in the range 5%–10%.

For a few of the galaxies of Table 2, some special circumstances are present or special treatment was required. For NGC 2841, the very faint line emission produces large, and highly uncertain, A_V values. For NGC 5033, no Hα image is available; the uncorrected Paα can be up to 70% underestimated for the largest A_V measured in our sample ($A_V \sim 4$ mag), and, therefore, this galaxy is excluded from all fits reported below.

In Holmberg IX, Hα emission is detected in two of the three selected regions; for one of these two regions, 24 μm emission is also detected, at the $\sim$2.5 σ level. A strong 24 μm detection is present in the third region, together with the only 8 μm detection in the field; because of the absence of hydrogen line emission and of the extended nature of the broadband emission, this source is identified with one of the background sources discussed in § 4.1. For the two regions with Hα emission, only upper limits can be derived for the Paα and 8 μm emission. The presence of Hα emission provides a lower limit to the Paα line intensity for the zero-extinction case (after including the uncertainty on the Hα measurement itself). We have taken the range between this lower limit and the upper limit measured from the *HST* NICMOS images to be our fiducial range of values for Paα, and therefore we report the middle values (in logarithmic scale) as measurements, rather than use the actual upper limits.

In NGC 5408, the brightest, and most extended, line-emitting region is only partially imaged by NICMOS. The Paα image is therefore used only to derive a typical A_V value for the region, using small-aperture photometry and the matching Hα measurements. The A_V value derived in this way is then applied to the Hα emission of the entire, extended region, for which a larger than nominal (17.1″ diameter) aperture is used, not only for Hα, but also for the 8 and 24 μm emission. The other two regions in this galaxy are treated with the nominal procedure described in § 4.1.

5. STARBURST GALAXIES

Our baseline sample of 220 H II knots is augmented with 10 local low-metallicity starburst galaxies and 24 LIRGs from Engelbracht et al. (2005) and Alonso-Herrero et al. (2006), respectively, in order to verify that trends and correlations observed for star-forming regions within galaxies can also be applied to galactic-scale ($\sim$kpc) star formation. In this context, starbursts are defined as galaxies with a central, connected star-forming region whose energy dominates the light output in the wave bands of interest.

The low-metallicity starbursts and the LIRGs also expand the MIR and line emission LSD parameter space of the low- and high-metallicity H II knots, respectively, by more than an order of magnitude at the high end.

5.1. *Low-Metallicity Starburst Galaxies*

As part of the *HST* NICMOS SNAP-9360, about 40 nearby starburst galaxies were observed. Of these, 13 also have *Spitzer* imaging as part of the MIPS and IRS GTO observations (Engelbracht et al. 2005). The main characteristics and measurements for 10 of these galaxies are listed in Tables 3 and 4. The three remaining galaxies, NGC 3079, NGC 3628, and NGC 4861, are omitted from the present analysis for the following reasons. For NGC 4861, the *HST* NICMOS pointing targeted the relatively quiescent center of this galaxy, rather than the peripheral giant H II region. The other two galaxies, NGC 3079 and NGC 3628, have extended optical line and MIR emission: about 40% and 60% of the emission is outside of the FOV imaged by *HST* NICMOS; corrections for the fraction of light in the Paα line outside of the observed frame would be thus substantially larger than the typical uncertainties in the measurements.

The data for the galaxies in Table 3 were reduced in the same fashion as the SINGS galaxies discussed in §§ 2 and 3. In particular, the *HST* NICMOS images, which are presented here for the first time, were treated following the same procedure as in § 3.2. The main difference between the H II knots in the SINGS galaxies and the local starbursts is in the photometry: integrated flux values encompassing the *entire central starburst* (the dominant source of emission at the wavelengths of interest) are derived for the latter sample. The integrated measurements at 8 and 24 μm are from Engelbracht et al. (2005) and are reported in Table 4.

The Paα measurements (Table 4) are performed using the aperture sizes listed in Table 3 and are corrected for the Galactic foreground extinction (fourth column of Table 3), but not for internal extinction. We expect the internal extinction to represent a small effect on the Paα flux in these mostly low-metallicity galaxies (compare with Fig. 2). An exception may be represented by SBS 0335−052, for which Houck et al. (2004) measure $A_{9.7\ \mu\mathrm{m}} \sim 0.5$ mag. If the region of silicate absorption is coincident with the region of line emission, this would correspond to $A_{\mathrm{Pa}\alpha} \sim 2$ mag. Given the uncertainty in the spatial colocation of the dust-hidden source detected by Houck et al. (2004) and the main source(s) of the Paα emission and the fact that the introduction of an extinction correction for one of the galaxies does not impact our conclusions, we do not perform the correction.

5.2. *Luminous Infrared Galaxies*

HST NICMOS Paα data and extinction corrections, as well as information on the physical extent of the star-forming area for each of the 24 LIRGs used in this analysis, are presented in Alonso-Herrero et al. (2006); the reader is referred to that work for details. Infrared measurements at 25 μm from *IRAS* and

TABLE 3
CHARACTERISTICS OF THE STARBURST GALAXIES

Name	Morphology[a]	v_H[a] (km s^{-1})	$E(B-V)_G$[a]	R[b] (arcsec)	$12+\log(\mathrm{O/H})$[c]
UGCA 292	Im IV–V	308	0.016	5.1	7.2
SBS 0335−052	BCG	4043	0.047	4.1	7.3
HS 0822+3542	BCG	732	0.047	4.1	7.4
VII Zw 403	Pec.	−103	0.036	6.1	7.7
UM 461	BCD/Irr	1039	0.018	5.1	7.8
Mrk 1450	Comp.	946	0.011	5.1	8.0
II Zw 40	BCD	789	0.820	11.2	8.1
NGC 5253	Im pec	407	0.056	14.2	8.2
NGC 2537	SB(s)m	431	0.054	8.1	8.7
NGC 2146	SB(a)ab	893	0.096	13.8	8.4–9.0

[a] Galaxy morphology, heliocentric velocity, and foreground Galactic color excess are from the NASA/IPAC Extragalactic Database (NED). The Galactic color excess, $E(B-V)_G$, is from Schlegel et al. (1998).
[b] Radius of the region of active star formation, as measured in the NICMOS images.
[c] Oxygen abundances, reproduced from Table 1 of Engelbracht et al. (2005). For UGCA 292, the oxygen abundance is from Pilyugin (2001); for NGC 5253 from Martin (1997); for NGC 2146 the line ratios of Ho et al. (1997) have been converted to a range of possible oxygen abundances using the strong-lines method of Kewley et al. (2002).

distances for each galaxy are from Sanders et al. (2003) and Surace et al. (2004). At the time of this writing, no 8 μm emission measurements are available for these galaxies. The LIRGs' metallicities are characteristic of our high-metallicity H II knot sample (Alonso-Herrero et al. 2006). Photometry for these galaxies, as in the case of the local starbursts (§ 5.1), includes the entire line-emitting and IR-emitting galactic region; thus, the measurements are integrated galaxy values.

6. ANALYSIS AND RESULTS

Photometric measurements for the 220 H II knots, the local low-metallicity starbursts, and the LIRGs are shown in Figures 3 and 4, where the infrared LSD in the two MIR wave bands is shown as a function of the extinction-corrected Paα LSD.

One characteristic immediately apparent in Figures 3 and 4 is the overall correlation between the infrared LSDs and the Paα LSD (Figs. 3*a* and 4*a*), although the scatter is nonnegligible in both cases (Figs. 3*b* and 4*b*). The correlations appear especially significant for the high-metallicity H II knots (the most numerous subsample among those under analysis here) and span a little over 2 orders of magnitude in Paα LSD. Bilinear least-squares fits through the high-metallicity data points yield

$$\log S_{8\,\mu\mathrm{m,dust}} = (0.94 \pm 0.02)\log S_{\mathrm{Pa}\alpha,\mathrm{corr}} + (4.80 \pm 0.85), \quad (2)$$

$$\log S_{24\,\mu\mathrm{m}} = (1.23 \pm 0.03)\log S_{\mathrm{Pa}\alpha,\mathrm{corr}} - (6.88 \pm 0.97), \quad (3)$$

where $S_{\mathrm{Pa}\alpha,\mathrm{corr}}$ is the extinction-corrected Paα LSD. Equation (3) accounts effectively for the trend of the LIRGs, although these data were not used in the fitting procedure.

The scatter of the data points about the best-fit lines of equations (2) and (3) is approximately the same, with $\sigma = 0.3$ dex (Figs. 3*b* and 4*b*). Thus, the 1 σ scatter is about a factor of 2 for the high-metallicity regions.

A potential source of bias in equations (2) and (3) is the large range of distances that our sample covers, about a factor of 6 for the high-metallicity galaxies. Our fixed photometric aperture of 13″ diameter thus probes regions that are about 30 times different in area between the nearest and the farthest targets in the high-metallicity subsample, i.e., from 0.04 kpc^2 at 3.5 Mpc to 1.12 kpc^2 at 17 Mpc (for the most distant galaxy in our sample, NGC 4125, located at 21 Mpc, only the central Seyfert 2 nucleus is detected and is excluded from the analysis). Although we remove the background from each photometric measurement, uncertainties in this subtraction will affect the farthest targets more strongly than the closest ones, if H II regions/complexes have constant sizes of ≈100–200 pc. Furthermore, we may expect that our fixed aperture photometry may dilute the LSDs of the more distant regions, for the extreme hypothesis that only one H II region is contained in each aperture. We have tested the impact of these effects by looking at the distribution of the ratios $S_{8\,\mu\mathrm{m,dust}}/S_{\mathrm{Pa}\alpha,\mathrm{corr}}$ and $S_{24\,\mu\mathrm{m}}/S_{\mathrm{Pa}\alpha,\mathrm{corr}}$ as a function of galaxy distance (Fig. 5). For the high-metallicity subsample, nonparametric (both Spearman and Kendall) tests show that the data are uncorrelated with the galaxy's distance, suggesting that there is no obvious bias in our analysis.

Both the 8 and 24 μm LSDs of intermediate- and low-metallicity regions are deficient relative to the extrapolation of the best-fit

TABLE 4
MEASUREMENTS OF THE STARBURST GALAXIES

Name	$\log S_{\mathrm{Pa}\alpha}$[a] (ergs s^{-1} kpc^{-2})	$\log S_{8\,\mu\mathrm{m,dust}}$[a] (ergs s^{-1} kpc^{-2})	$\log S_{24\,\mu\mathrm{m}}$[a] (ergs s^{-1} kpc^{-2})
UGCA 292	38.44	40.11 ± 0.33[b]	39.71 ± 0.42
SBS 0335−052	39.59	41.67 ± 0.02	41.97 ± 0.10
HS 0822+3542	39.12	39.48 ± 0.21	40.68 ± 0.11
VII Zw 403	39.2	40.48 ± 0.24	41.34 ± 0.11
UM 461	39.42	40.57 ± 0.09	41.43 ± 0.10
Mrk 1450	39.72	40.73 ± 0.09	41.64 ± 0.10
II Zw 40	40.28	41.59 ± 0.05	42.4 ± 0.10
NGC 5253	40.37	42.34 ± 0.07	42.93 ± 0.10
NGC 2537	39.94	42.02 ± 0.16	41.94 ± 0.10
NGC 2146	40.64	43.44 ± 0.03	43.24 ± 0.10

[a] The LSD at Paα, 8 μm, and 24 μm in the starburst regions, with radius listed in Table 3. The Paα LSDs are from the *HST* SNAP program 9360 and are only corrected for foreground Galactic extinction (Table 3). Measurement uncertainties for $S_{\mathrm{Pa}\alpha}$ are around 15%–20%. The LSDs in the *Spitzer* bands are "whole galaxy" measurements, corrected to infinite aperture, although in all cases the central starburst (measured in the NICMOS images) is the dominant contributor to the flux.
[b] The 8 μm emission from this galaxy is affected by a latent image from a previous observation. Every effort has been made to remove the contaminating latent image from the measurement, but the presence of some small remnant contamination cannot be excluded.

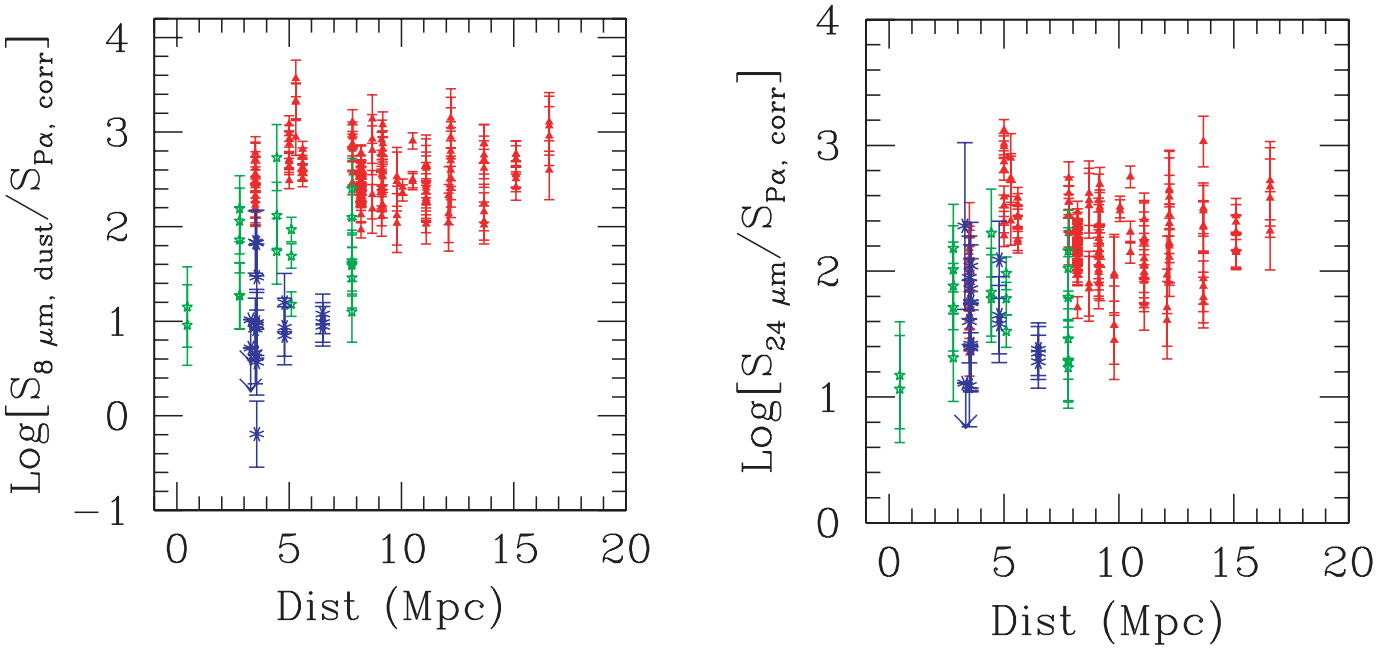

FIG. 5.—Ratio of the MIR to the extinction-corrected Paα LSDs, as a function of the galaxies' distances, for the 8 μm (*left*) and the 24 μm (*right*) H II knot measurements, respectively. Background sources and nonthermal sources are not included. In both panels, the high-metallicity data points are consistent with no correlation of the ratio as a function of distance, implying that the correlations between the MIR emission and the Paα emission are not driven by distance effects. The 8 μm emission of the intermediate- and low-metallicity H II knots remains on average deficient relative to that of the high-metallicity data also when only galaxies at similar distances are considered (thus, flux measurements are performed in similar-size regions). With the possible exception of NGC 6822, which is at a distance of only 0.47 Mpc and shows lower than average values for its metallicity bin, the observed 8 μm emission deficiency in metal-poor regions is not an effect of a bias in the size of the regions that are being measured.

lines for the high-metallicity regions (Figs. 3 and 4). The deficiency is far more pronounced in the case of $S_{8\ \mu\mathrm{m,dust}}$, a fact already noted in a number of previous investigations (e.g., Engelbracht et al. 2005; Galliano et al. 2005; Hogg et al. 2005; Rosenberg et al. 2006; Draine et al. 2007). A potential source of concern in this case is that the high-metallicity subsample has a higher mean distance than the intermediate- and low-metallicity ones (Fig. 5). Helou et al. (2004) have shown that the 8 μm emission is brighter at the edges of an H II region (i.e., in the PDR) than at its center. Our fixed aperture photometry could therefore underestimate the 8 μm flux from the low-metallicity regions, if the apertures are not large enough to sample the entire area surrounding the H II knot. However, Figure 5 shows that the 8 μm emission is deficient in the intermediate- and low-metallicity subsamples relative to the high-metallicity one even when galaxies at comparable distances are considered. The only potential exception is NGC 6822, the closest galaxy to the Milky Way in our sample, which, at a distance of 0.47 Mpc, could suffer from the effect of having too small an aperture applied to the 8 μm emission measurements; indeed, its mean value is lower (although not statistically significantly) than the average of the other data in the same metallicity bin.

The trend of the $S_{8\ \mu\mathrm{m,dust}}/S_{24\ \mu\mathrm{m}}$ ratio as a function of $S_{\mathrm{Pa}\alpha\mathrm{,corr}}$ (Fig. 6) highlights the decrease of the 8 μm LSD for decreasing metallicity and also shows that the effect is independent of the number of ionizing photons in the region. The latter suggests that (1) our aperture sizes are large enough to encompass both the H II regions and the surrounding PDRs, as noted above; and (2) in these large regions the dependence of the 8 μm to 24 μm ratio on the LSD of the H II region/complex that heats the dust is a small effect relative to the effect of metallicity. The decrease of the 8 μm to 24 μm LSD ratio as a function of increasing Paα LSD in the high-metallicity points (i.e., at roughly constant metallicity) indicates that the component of thermal equilibrium dust contributing to the 24 μm emission is increasing in strength (the dust is in thermal equilibrium and "warmer" at higher ionizing photon densities; see Helou 1986; Draine & Li 2007). An additional contribution may also come from an increased destruction rate of the 8 μm dust emission for increasing starlight intensity (Boulanger et al. 1988).

As suggested by Kennicutt et al. (2007), the combination of measurements at Hα and 24 μm can provide insights into both the unobscured and obscured regions of star formation. We have combined linearly the observed Hα and 24 μm LSDs and scaled them to the Paα LSD. The best-fit line through the data is

$$\log S_{\mathrm{Pa}\alpha\mathrm{,corr}} = (0.98 \pm 0.02)\log\left(aS_{\mathrm{H}\alpha\mathrm{,obs}} + bS_{24\ \mu\mathrm{m}}\right) + (0.73 \pm 0.93), \quad (4)$$

where a is the intrinsic Paα/Hα ratio, and thus is dictated by atomic physics and is only moderately dependent on metallicity ($a = 0.128$, 0.118, and 0.114 for the high-, intermediate-, and low-metallicity data, respectively; see § 3.2). The coefficient b for the 24 μm LSD has been empirically rescaled to bring the sum of the optical and IR LSDs in agreement with the Paα one ($b = 0.0040$, 0.0037, and 0.0036 for the high-, intermediate-, and low-metallicity data points, respectively; Fig. 7). The best fit from equation (4) gives $b/a = 0.031 \pm 0.006$, and this ratio is independent of metallicity. Equation (4) is, within the uncertainties, consistent with a linear relation with null intercept between the two quantities, as expected if the right-hand side expression is a measure of the ionizing photon rate, like $S_{\mathrm{Pa}\alpha\mathrm{,corr}}$. The linearity of the relation is by construction, as the requirement is to approach unity as much as possible for all the combined data, but the null intercept has not been fixed a priori; furthermore, the

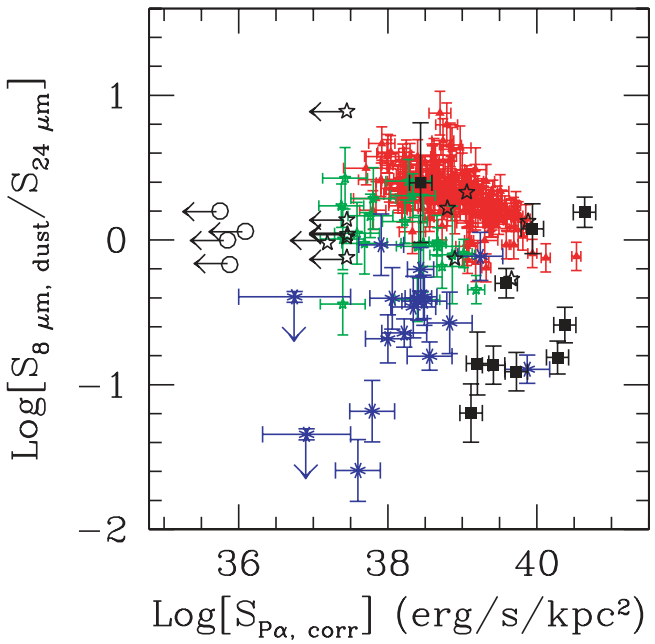

FIG. 6.—Ratio of the 8 μm to 24 μm LSD as a function of the extinction-corrected Paα LSD for the 220 H II knots and for the local starbursts. Symbols and colors are as in Fig. 3. The deficiency of the 8 μm emission relative to the 24 μm emission for the low-metallicity data points is independent of the average ionizing photon rate in the region. The decrease of the 8 μm to 24 μm LSD ratio as a function of increasing Paα LSD for the high-metallicity points indicates that the component of thermal equilibrium dust contributing to the 24 μm emission is increasing in strength (the dust is in thermal equilibrium and "warmer" at higher ionizing photon densities; see Helou 1986; Draine & Li 2007). A contribution to the decrease of the 8 μm emission due to increased destruction rate of the carriers for increasing starlight intensity (Paα LSD) may also be present (Boulanger et al. 1988).

ratio b/a was left as a free parameter in the analysis, and its constant value is a result (not an input).

Interestingly, the high-metallicity data points show approximately the same dispersion around the mean trend of equation (4) as they do for equations (2) and (3), with a 1 $\sigma \sim 0.3$ dex. In the case of the combined optical/MIR, the dispersion is the same whether the high-metallicity data points alone or all data points are included in the statistical analysis (Fig. 7*b*). Conversely, for the two MIR LSDs the dispersion is measured for the high-metallicity data points only and increases substantially (on one side) when the intermediate- and low-metallicity data points are included in the statistics (Figs. 3*b* and 4*b*). These considerations do not include the LIRGs, which in Figure 7 show evidence of having higher combined optical/MIR LSDs than inferred from the extrapolation of equation (4). A possible explanation for this effect is discussed in § 7.

As already discussed in Kennicutt et al. (2007), the sum on the right-hand side of equation (4) can be interpreted as a representation of the dust extinction–corrected Hα luminosity or LSD as

$$S_{\mathrm{H}\alpha,\mathrm{corr}} = S_{\mathrm{H}\alpha,\mathrm{obs}} + (0.031 \pm 0.006) S_{24\,\mu\mathrm{m}}. \quad (5)$$

The proportionality coefficient for the 24 μm luminosity is ~20% smaller than that derived for NGC 5194 alone (Kennicutt et al. 2007), which is within the 1 σ uncertainty. This small difference is likely due to the larger variety of galaxies used in the present work, which provides a dynamical range in LSD about an order of magnitude larger than in the NGC 5194 case.

The proportionality coefficient for the 24 μm emission in equations (4) and (5), $b/a = 0.031$, is independent of metallicity. This suggests that in the $S_{24\,\mu\mathrm{m}}$ versus $S_{\mathrm{Pa}\alpha,\mathrm{corr}}$ plane the observed deviations of the intermediate- and low-metallicity data from the best fit for the high-metallicity data points are simply

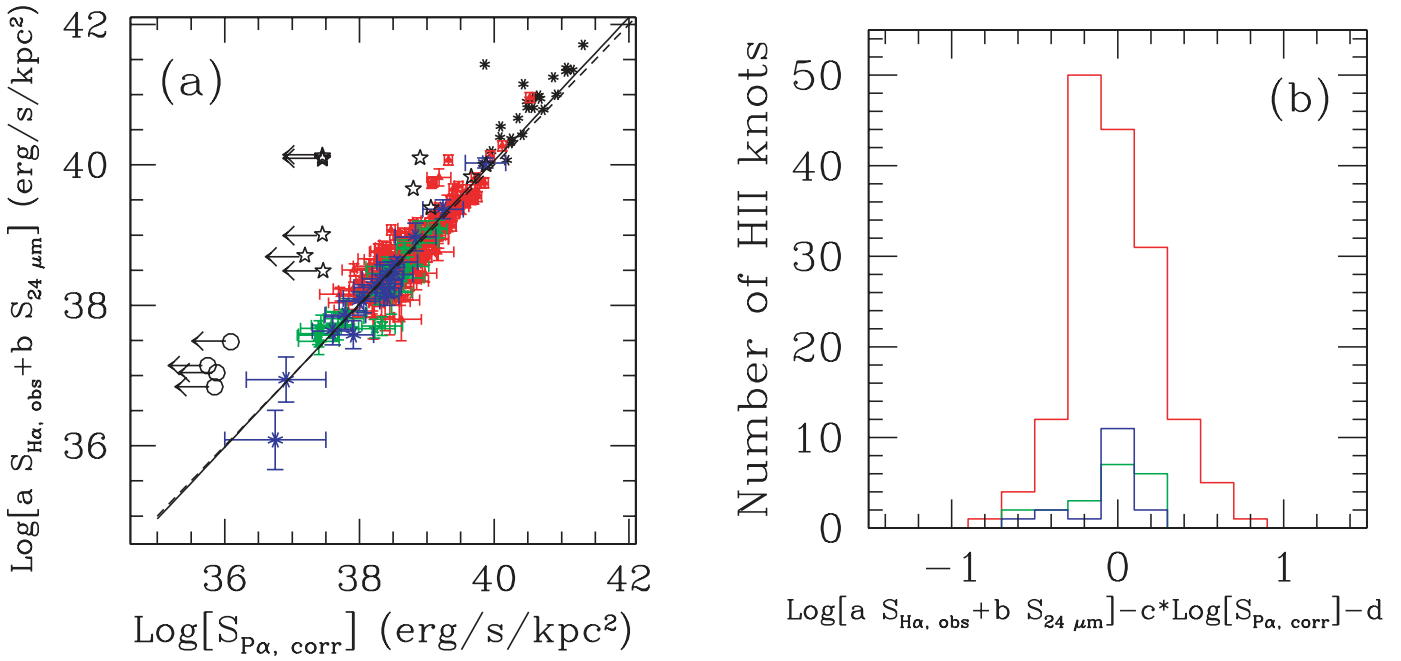

FIG. 7.—Same as Fig. 4, but for the linear combination of $\mathrm{H}\alpha_{\mathrm{obs}}$ and 24 μm LSD (eq. [4]). Symbols are as in Figs. 3 and 4. (*a*) Data for the H II knots and the LIRGs. The best-fit line through the high-metallicity H II knots (*solid line*) is not significantly different from a linear relation with slope of unity (*dashed line*). (*b*) Histogram of the deviation of the H II knot data in panel *a* from the best-fit line through the high-metallicity data (the solid line in panel *a*). Unlike Figs. 3 and 4, the histograms of the intermediate- and low-metallicity data points have not been multiplied by a factor of 2. The values of the *x*-label parameters (*c, d*) are derived from eq. (4) and are $c = 1.02 \pm 0.02$ and $d = -0.74 \pm 0.97$.

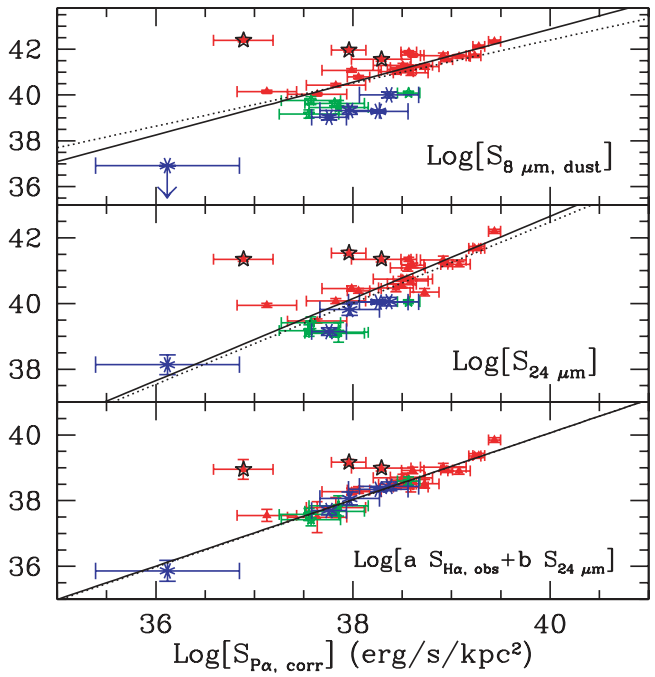

FIG. 8.—MIR or combined optical/MIR LSD as a function of the extinction-corrected Paα LSD, averaged over the entire central region covered by the *HST* NICMOS observations, for each of the star-forming galaxies from Table 1 (§ 4.1). The three panels show on the vertical axis, from top to bottom, the 8 μm, 24 μm, and the linear combination of Hα and 24 μm LSDs in logarithmic scale, as indicated by the label at the bottom right corner of each plot; the vertical axis has the same units as the horizontal axis, ergs s^{-1} kpc^{-2}. Each *HST* NICMOS image is about 50″ in size, except for NGC 5194, where a region of 144″ in size has been observed. Color coding of each galaxy is the same as the H II knots in Fig. 3. The solid lines are the best linear fit through the high-metallicity (*red triangles*) data, after excluding the Seyfert 2–dominated fluxes of NGC 4569, NGC 4736, and NGC 5195 (marked as black stars), thus leaving 19 independent data points. The dotted lines are the best fits through the high-metallicity H II knots from Figs. 3, 4, and 7 for $S_{8\,\mu\mathrm{m,dust}}$, $S_{24\,\mu\mathrm{m}}$, and $S_{\mathrm{H}\alpha\,,\mathrm{obs}} + S_{24\,\mu\mathrm{m}}$, respectively.

due to the progressively lower dust content of the interstellar medium (ISM) for decreasing metallicity (§ 7). No other effect beyond the simple increase in the medium's transparency is required. Indeed, most of the contribution to $S_{\mathrm{H}\alpha\,,\mathrm{corr}}$ comes from the observed Hα emission at low $S_{\mathrm{Pa}\alpha\,,\mathrm{corr}}$ LSDs (low dust systems) and, vice versa, it is mainly contributed by the 24 μm emission at the high LSD end of our sample (dusty systems).

Similar correlations as those seen for the H II knots within galaxies exist between the integrated LSDs of the galaxies' centers (§ 4.1). Figure 8 shows the trends for the 33 star-forming galaxies in our main sample. For the combined optical/MIR LSDs, a linear fit through the integrated data points of the high-metallicity galaxies is consistent, within 1 σ, with the best-fit lines through the individual H II knots, in both slope and intercept (Fig. 8, *bottom panel*). For the 24 μm LSD, the slope of the linear fit is consistent (again within 1 σ) with that of the individual H II knots, and the intercept is consistent (within 0.1 σ) with the value expected by simply rescaling the H II knots' mean LSD for the larger area used in the integrated measures. The results for both the 24 μm and the combined optical/MIR integrated measures suggest that within the central areas covered by the NICMOS observations any diffuse 24 μm emission contributing to the measured LSD is matched by diffuse Paα LSD with comparable intensity. This, of course, does not mean that diffuse 24 μm emission is not present; indeed, such diffuse emission has been observed in the SINGS galaxies (Dale et al. 2007). Our result simply implies that such diffuse 24 μm emission traces the diffuse ionized emission, at least within the central galaxy regions sampled by our data.

A more complicated scenario appears for the 8 μm LSD: a best-fit line through the high-metallicity integrated regions produces a higher slope (1.16 ± 0.09) than derived for the individual H II knots. The difference is marginally significant (2.2 σ) but implies that the 8 μm LSD is higher by about a factor of 2 over what is expected from a simple rescaling of areas at the high-luminosity end.[21] A visual inspection of the images shows that the galaxies with low 8 μm LSDs generally have line and MIR emission that is centrally concentrated or coming from thin, almost edge-on disks or annuli located in the central 50″, while at the high 8 μm LSD end galaxies tend to have a more homogeneous distribution of H II knots.

7. COMPARISON WITH MODELS

To help clarify the nature of some of the characteristics of the observed correlations, this section is devoted to the comparison of our data with simple models that exploit the energy balance between the stellar light absorbed by dust at UV, optical, and near-infrared wavelengths and the light emitted by the dust in the MIR and far-infrared. The details of the models are presented in the Appendix, in addition to a discussion on limitations to their use and applicability. Here we provide a brief summary of those models.

The basic approach adopts a range of plausible stellar populations for our H II knots (and starburst galaxies), in terms of star formation histories, stellar population ages, and metallicities (2005 update of Starburst99;[22] Leitherer et al. 1999). Simple assumptions are also made for the ISM structure and metal content. The intrinsic stellar populations are then dust attenuated according to empirical recipes (Calzetti et al. 1994, 2000; Meurer et al. 1999; Calzetti 2001) to provide a "predicted" infrared emission, S_{IR}. As the stellar populations probed in our analysis range from groupings of a few to several H II regions for the H II knots to populations with extended star formation histories in the case of starbursts and LIRGs, both instantaneous bursts and constant star formation populations are included. The total infrared emission will, in general, depend not only on the adopted stellar population but also on the extinction curve and the dust geometry. Since for the last two parameters we make a simplifying assumption and use the prescription of Calzetti (2001), the impact of varying the dust geometry is discussed in § A4. For the SED of the infrared emission, S_{IR}, we adopt the model of Draine & Li (2007), according to which the fraction of IR power emerging in the IRAC 8 μm and MIPS 24 μm bands is a function of the starlight intensity. We determine (§ A2) the range of starlight intensities corresponding to the model stellar populations we are considering, so as to obtain a direct correlation between the Paα LSD and the fraction of IR light emerging in the two MIR bands. Since our H II knots follow the well-known correlation between SFR and extinction (§ A1; see also Wang & Heckman 1996; Heckman et al. 1998; Hopkins et al. 2001; Calzetti 2001; Moustakas et al. 2006), which we parameterize as a relation between color excess $E(B-V)$ (§ 3.2) and the ionizing photon rate per unit area Σ_{ion}, we use this relation to link the stellar population models to the dust attenuation model and eliminate 1 dof in our models. Model parameters that we allow to vary are the star formation history of the stellar populations (bursts or constant star formation), their age (0–10 Myr for instantaneous

[21] For the "integrated" diffuse emission, the extended source aperture correction provided by Jarrett (2006) has been used.

[22] See http://www.stsci.edu/science/starburst99.

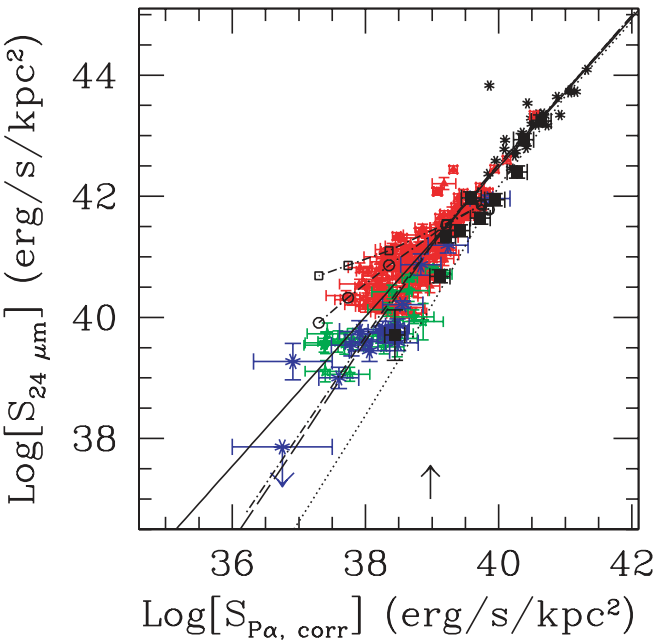

FIG. 9.—LSD at 24 μm as a function of the extinction-corrected Paα LSD for the same data points as Fig. 4 (after removal of the Seyfert 2 nuclei, the foreground and background sources, and the NGC 5033 H II knot data, leaving 164 independent data points in the high-metallicity H II knot subsample). The solid line shows the best linear fit through the high-metallicity H II knots, from Fig. 4. Models of infrared and ionized gas emission are superimposed on the data, for a variety of star formation histories, stellar population ages, and metallicities (see the Appendix). Models with solar metallicity ($Z = Z_\odot$) ISM and stellar populations include 100 Myr old constant star formation (SFR/area = 4×10^{-5} to 4 $M_\odot$ yr^{-1} kpc^{-2}; *long-dashed line*); instantaneous burst with variable mass (10^3–10^8 $M_\odot$ kpc^{-2}); and color excess and constant age of 4 Myr (*dot-dashed line*); instantaneous bursts with constant mass (10^6 $M_\odot$ kpc^{-2}) and variable age and both variable color excess (*dot-dashed line with open circles*) and constant color excess [$E(B-V) = 2$ mag; *dot-dashed line with open squares*]. The circles and squares mark the population ages: 0.01, 2, 4, 6, 8, and 10 Myr (*right to left*). The dotted line marks a 1/10 $Z_\odot$ model of constant star formation over the past 100 Myr. The upward-pointing arrow marks the approximate luminosity where the transition between single-photon heating and thermal equilibrium heating for the dust begins to occur.

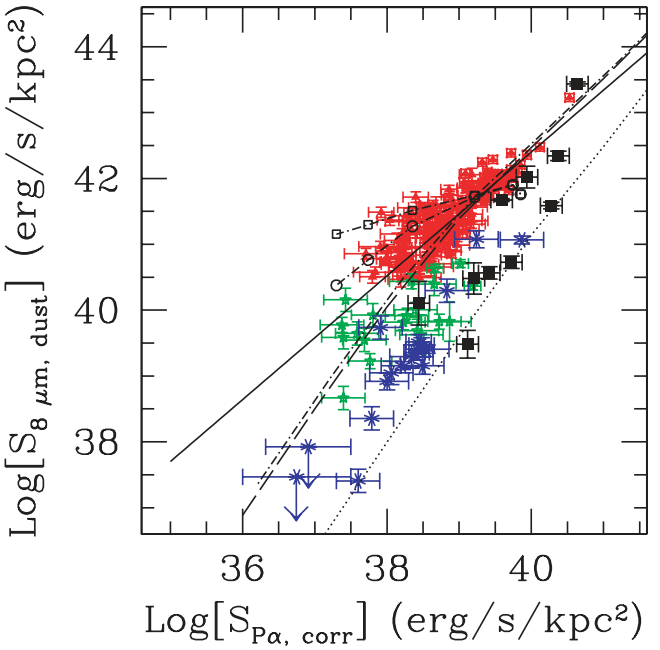

FIG. 10.—LSD at 8 μm as a function of the extinction-corrected Paα LSD for the same regions/galaxies as Fig. 9 (minus the LIRGs). The solid line is the best linear fit through the high-metallicity H II knots, as in Fig. 3. Models of infrared and ionized gas emission are the same as in Fig. 9.

bursts, the range chosen to ensure the presence of a significant ionizing photon rate; Leitherer et al. 1999; 6–100 Myr for constant star formation), the mass (10^3–10^8 $M_\odot$) or SFR (4×10^{-5} to 4 $M_\odot$ yr^{-1}) of the stellar cluster(s) associated with the H II knot or starburst galaxy, and the metallicity of both the population and the ISM (0.1–1 $Z_\odot$).[23] Figures 9–11 show the basic results from the comparison between the models described so far and our data for the 8 μm, 24 μm, and combined optical/MIR emission from H II knots and star-forming galaxies.

The larger than unity slope of the 24 μm versus Paα LSD (in log-log scale; Fig. 9) is a natural outcome of the models in the high LSD regime, $\log(S_{\mathrm{Pa}\alpha,\mathrm{obs}}) > 39$, and is an effect of the "hotter" IR SEDs for increasing starlight intensity. In other words, regions with higher Paα LSD emit proportionally more of their infrared energy into the 24 μm band because the peak of the IR SED moves toward shorter wavelengths (higher "effective" dust temperatures; see the Appendix and Draine & Li 2007).

The models also predict a slightly larger than unity value for the slope of the 8 μm LSD correlation, which is steeper than that of the H II knot data (Fig. 10) but is roughly consistent with the slope of the integrated measures.

The models account well for the linear relation of the combined optical/MIR LSD with the Paα LSD (Fig. 11), for LSDs $S_{\mathrm{Pa}\alpha,\mathrm{corr}} < 10^{40}$ ergs s^{-1} kpc^{-2}. At high LSD, the models for the combined LSDs depart from a linear relationship, as increased starlight intensities are expected to raise the temperatures of the larger grains so that the fraction of the absorbed energy reradiated

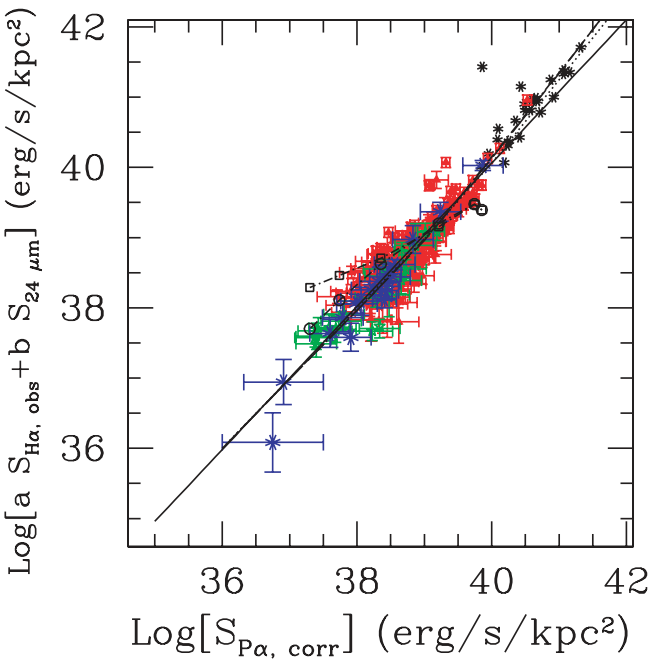

FIG. 11.—Combined optical/MIR LSD as a function of the extinction-corrected Paα LSD for the same data as in Fig. 9. The solid line is the best linear fit through the high-metallicity H II knots, as in Fig. 7. Models of infrared and ionized gas emission are the same as in Fig. 9.

[23] We adopt the oxygen abundance $12 + \log(\mathrm{O/H}) = 8.7$ as the solar metallicity value (Allende Prieto et al. 2001), which we take here as representative of our high-metallicity H II knots.

at 24 μm (which is, at these high LSDs, the dominant contribution to eq. [5]) increases. The LIRG data, which populate the high LSD regime in our plot, do indeed confirm observationally the deviation from the extrapolation of the best-fit line; they show a slope steeper than 1, in qualitative agreement with the models' expectations (Fig. 11).

At the high-luminosity end (LIRGs and brighter), an additional effect that can contribute to the deviation from the slope of unity observed in Figure 11 and the steeper-than-unity slope of Figure 9 is the competition between the dust and the gas for the absorption of some of the ionizing photons. In the high-luminosity regime, star formation occurs in environments of increasing density, e.g., ultracompact H II regions (Rigby & Rieke 2004), and the dust absorbs the ionizing photons before they can excite the gas. In this regime, standard extinction-correction methods become progressively less effective at recovering the intrinsic Paα emission and will produce an underestimate of the hydrogen emission line LSD at constant 24 μm LSD (§ A4). The impact of this effect on our data is unclear (and currently not included in our models), although it may be relatively small as the bulk of the observed trends is fully accounted for by our baseline model.

Instantaneous burst populations and constant star formation populations produce mostly degenerate models for all three MIR quantities (Figs. 9–11). A young (4 Myr old), instantaneous burst population in the mass range $\sim 10^3$–$10^8\ M_\odot$ provides similar model lines as a constant star formation model forming stars since 100 Myr and with SFR in the range 4×10^{-5} to $4\ M_\odot\ \mathrm{yr}^{-1}$.

However, even the high-metallicity H II knots in Figures 9 and 10 show a fairly large dispersion around the mean trends described above, with a clear increase of the dispersion around the mean $S_{8\ \mu\mathrm{m,dust}}$ and $S_{24\ \mu\mathrm{m}}$ values for $S_{\mathrm{Pa}\alpha\mathrm{,corr}} \leq 10^{39}$ ergs s^{-1} kpc^{-2}. Furthermore, in this Paα LSD regime, most of the 8 and 24 μm emission from the high-metallicity H II knots is located above the baseline model lines; i.e., the models underpredict the mean values of the MIR emission (Figs. 9 and 10). The "downward" curvature of the models is a direct product of the increasing transparency of the ISM for decreasing ionizing photon rate density and, from equation (A2), decreasing dust amount. With a more transparent medium, proportionally less IR radiation is produced. The medium is still thick to Lyman continuum photons, and the ionized hydrogen emission lines are still a measure of the total number of ionizing photons in the region. An additional parameter is thus required to account for both the large scatter of the data points around the mean trends and the large number of high-metallicity data points above the model lines for the $S_{8\ \mu\mathrm{m,dust}}$ and $S_{24\ \mu\mathrm{m}}$ LSD plots. *This second parameter appears to be the age of the stellar population*. Aging bursts between $\sim$0.01 and $\sim$8 Myr produce a decreasing number of ionizing photons, while at the same time remaining luminous at UV–optical wavelengths (the major contributors to the IR emission). Figures 9–11 show that the "flaring" of the high-metallicity H II knot data points around the mean value for decreasing Paα LSD is compatible with the flaring of the aging burst models. Such aging populations can also account for the data points above the mean trends in Figures 9 and 10.

The presence of aging bursts is a sufficient (and physically expected), but not a necessary, condition to account for the dispersion in the data. As briefly discussed in the Appendix (§ A4), different assumptions from our default one about the average dust geometry can also produce a higher MIR emission than our fiducial model lines. For instance, the presence of ultracompact H II regions within our H II knots will produce higher IR emission at fixed $S_{\mathrm{Pa}\alpha\mathrm{,corr}}$ than expected from the models. This is a consequence of the higher opacity of such regions, for which the use of the Hα/Paα ratio to recover the intrinsic line fluxes will lead to an underestimate of the intrinsic Paα luminosity in the region. Recently, Dale et al. (2007) have shown that for local star-forming galaxies the UV/IR ratio is heavily determined by the morphology of the 24 μm dust emission, in particular by the "clumpiness" of such emission, which therefore determines the escape fraction of UV photons from star-forming regions. A clumpy configuration of dust is, however, well described by the empirical recipes of dust extinction and attenuation used in the present work (Calzetti et al. 1994; Meurer et al. 1999; Calzetti 2001).

For the combined optical/MIR LSD, the models are degenerate as a function of metallicity (Fig. 11). This is not surprising if the main driver of the discrepancy between the high- and low-metallicity $S_{24\ \mu\mathrm{m}}$ at fixed Paα LSD is the larger medium transparency, i.e., lower dust column density, in the lower metallicity data (eqs. [A2] and [A4]). This is indeed the case (Fig. 9): the separation at low Paα LSD between the solar metallicity and the 1/10 solar metallicity model lines is mostly due to the metallicity scaling factor in equations (A2) and (A4) and, to a much smaller extent, to the difference in metallicity of the two stellar populations. The 1/10 metallicity model line in Figure 9 provides the lower envelope to the data; most of the galaxies in our sample are above 1/10 solar in metallicity and thus are expected to lie above this model line.

This result lends credence to the use of a combination of $S_{24\ \mu\mathrm{m}}$ and $S_{\mathrm{H}\alpha\mathrm{,obs}}$ (eq. [5] and Kennicutt et al. 2007) as an effective tool for measuring the ionizing photon rates and, ultimately, SFRs, at least up to Paα LSDs $\approx 10^{40}$–10^{41} ergs s^{-1} kpc^{-2}. In this framework, $S_{24\ \mu\mathrm{m}}$ probes the obscured star formation, and the only metallicity effects are those induced by reduced opacity; conversely, $S_{\mathrm{H}\alpha\mathrm{,obs}}$ probes that part of the star formation unabsorbed by the dust, independent of the gas metallicity. The behavior of the models in Figure 11 shows little difference between different parameter choices, at least within our data uncertainties, and they reproduce the main trend of the data reasonably well.

The discrepancy observed between the high-metallicity and low-metallicity $S_{8\ \mu\mathrm{m,dust}}$ data at fixed Paα LSD requires one additional ingredient, together with the increased transparency of the medium. Draine & Li (2007) have suggested that the fraction of low-mass PAH molecules present in the dust mixture decreases for decreasing metallicity. In the Appendix we show that the two ingredients (increased medium transparency and decrease of low-mass PAH molecule fraction) provide comparable contributions to the depression of the 8 μm emission, and the two together produce the expected lower envelope to the data points in Figure 10.

8. DISCUSSION

The scope of this study has been to investigate the extent of the regime of applicability of MIR emission as an SFR tracer, to use models to reproduce the main characteristics of the data, and to investigate reasons for any limitation we have encountered. The general trend of MIR LSDs to correlate with the ionizing photon rates or with SFR tracers had already been found by a number of authors (for some of the most recent results, see Roussel et al. 2001; Förster Schreiber et al. 2004; Boselli et al. 2004; Calzetti et al. 2005; Wu et al. 2005; Alonso-Herrero et al. 2006).

8.1. *The Combined Optical/MIR SFR Indicator*

Of the three indicators investigated here, the linear combination of the observed Hα and the 24 μm emission is the one

most tightly correlated with the extinction-corrected Paα emission. The linear relation between the combined optical/MIR emission and the SFR as traced by $S_{\mathrm{Pa}\alpha,\mathrm{corr}}$ is common to all galaxies investigated, independent of their metallicity. The most straightforward interpretation (Kennicutt et al. 2007) is that the 24 μm emission traces the dust-obscured star formation, while the observed Hα emission traces the unobscured one. Thus, the combination of the two recovers all the star formation in a region. This interpretation is confirmed by the models investigated in the previous section, which also suggest the trend to be relatively independent of the characteristics of the underlying star-forming population. The deviations from the linear relation (i.e., from a slope of 1 in log-log scale; Fig. 11) observed at luminosities larger than $S_{\mathrm{Pa}\alpha,\mathrm{corr}} > 10^{40}$–$10^{41}$ ergs s^{-1} kpc^{-2} are also consistent with the models' expectations: as the 24 μm emission starts dominating the luminosity budget, the same physical mechanism producing the $S_{24\,\mu\mathrm{m}}$ versus $S_{\mathrm{Pa}\alpha,\mathrm{corr}}$ trend also produces that of the combined optical/MIR indicator. We speculate that this mechanism (see below) is the emission from grains with approximately steady temperatures, rather than transiently heated grains, that come into play at high dust temperatures, and which causes the ratio of 24 μm/IR to deviate from a constant value at low starlight intensities to one that increases with the starlight intensity.

Using our baseline best-fitting model of 100 Myr constant SFR, for solar metallicity and the stellar IMF described in § A2, the conversion between SFR and Hα luminosity is

$$\mathrm{SFR}\left(M_\odot\ \mathrm{yr}^{-1}\right) = 5.3\times10^{-42} L(\mathrm{H}\alpha)_{\mathrm{corr}}\left(\mathrm{ergs\ s}^{-1}\right). \quad (6)$$

Variations of $\pm$20% over the constant in this relation are present for younger ages and metallicities down to $\sim\frac{1}{5}$ solar. The $\sim$50% difference between the calibration in equation (6) and that of Kennicutt (1998b) is mainly due to differences in the stellar IMF assumptions (59%), with a small contribution in the opposite direction coming from different assumptions on the stellar populations (100 Myr in our case vs. infinite age in Kennicutt [1998b], which gives a 6% decrease to the discrepancy given by the different IMFs).

Using equations (5) and (6),

$$\mathrm{SFR}\left(M_\odot\ \mathrm{yr}^{-1}\right) = 5.3\times10^{-42}[L(\mathrm{H}\alpha)_{\mathrm{obs}} + (0.031\pm0.006)L(24\ \mu\mathrm{m})], \quad (7)$$

where the luminosities are in ergs s^{-1} and $L(24\ \mu\mathrm{m})$ is expressed as $\nu L(\nu)$. This calibration does not change if the luminosities are measured over a substantial area of the galaxy (in our case the inner $\sim$0.8–5.1 kpc), rather than in smaller regions hugging the H II complexes that produce the ionizing radiation (Figs. 7 and 8). However, the potential nonlinearity at large LSDs is an important caveat.

8.2. *The* 24 μm *SFR Indicator*

Conversely, neither the 8 μm emission nor the 24 μm emission alone is linearly correlated with the number of ionizing photons that are measured in a region. The nonlinearity at high 24 μm luminosity is a direct consequence of the increasing dust temperature for more actively star-forming objects (Li & Draine 2001; Draine & Li 2007; Dale et al. 2001); higher dust temperatures correspond to higher fractions of the infrared emission emerging at MIR wavelengths. Following Draine & Li (2007), in the regime of low stellar intensities (low SFRs in our actively star-forming regions, or roughly $S_{\mathrm{Pa}\alpha,\mathrm{corr}} < 10^{39}$ ergs s^{-1} kpc^{-2}), most of the 24 μm emission comes from single-photon transient heating of small grains. In this case, the 24 μm photon flux is directly proportional to the stellar UV photon flux (or any other photon capable of single-photon heating). Thus, the 24 μm emission counts stellar UV/optical photons, while the Paα counts the Lyman continuum photons; since there is proportionality between the two types of photons, the expectation is for a linear scaling between 24 μm emission and Paα emission. However, this regime corresponds to the Paα LSD range where the decrease of dust opacity also decreases nonlinearly with the amount of stellar energy reprocessed by dust in the infrared. At high Paα LSDs, and hence high stellar intensities, the dust absorbing most of the stellar photons is warm. There is thus an increasing contribution to the 24 μm emission from larger, warm grains (the Wien side of the emission from grains), which leads to a nonlinear dependence of the 24 μm flux on the stellar flux. This is in agreement with the conclusions of Smith et al. (2007), which observe a decrease of the PAH/24 μm luminosity ratio for increasing 24 μm/70 μm luminosity ratio; this dependence is highly suggestive of an increasing contribution of warm dust to the 24 μm emission.

The observed nonlinearity in the 24 μm versus Paα relation, $S_{24\,\mu\mathrm{m}} \propto S^{1.23}_{\mathrm{Pa}\alpha,\mathrm{corr}}$, also argues against the case that the high LSD values measured of our apertures may be due to the cumulative contribution of many faint H II regions, rather than a few, increasingly bright H II regions. In the case of many faint H II regions (low stellar intensities and, therefore, single-photon heating) we should expect the 24 μm LSD to scale linearly with the Paα LSD at the high end. The observed nonlinear behavior argues in favor of the high-luminosity end to be contributed mainly by intrinsically bright regions, although the presence of apertures with many faint H II regions cumulatively giving a high LSD may still be present and contribute to the scatter of the data points around the mean trend.

At low metallicities, the deviation from a linear correlation is due to lower opacities for decreasing metal content, and thus column densities (Walter et al. 2007). The effect has been well known since the early *IRAS* observations (Helou et al. 1988): as the metallicity decreases, regions become proportionally more transparent and emit less in the infrared as a larger fraction of the radiation escapes the area unabsorbed by dust. This accounts for the underluminosity of the medium in low-metallicity regions in correspondingly intense ionizing fields. Using the 24 μm luminosity as an SFR tracer is thus subject to many caveats, including that lower metallicity sources will generally be more transparent than their metal-rich counterparts, and the infrared emission will typically underestimate their SFR by a factor of $\sim$2–4.

The nonlinear correlation between $S_{24\,\mu\mathrm{m}}$ and $S_{\mathrm{Pa}\alpha,\mathrm{corr}}$ requires some care for deriving SFR calibrations. From equation (3), and using equation (6), we derive an SFR density (SFR per unit area) calibration:

$$\Sigma_{\mathrm{SFR}}\left(M_\odot\ \mathrm{yr}^{-1}\ \mathrm{kpc}^{-2}\right) = 1.56\times10^{-35} \times\left[S_{24\,\mu\mathrm{m}}\left(\mathrm{ergs\ s}^{-1}\ \mathrm{kpc}^{-2}\right)\right]^{0.8104}. \quad (8)$$

In order to derive a calibration for SFRs, we convert our LSDs into luminosities, and the resulting best fit through the high-metallicity data points produces

$$\mathrm{SFR}\left(M_\odot\ \mathrm{yr}^{-1}\right) = 1.27\times10^{-38}\left[L_{24\,\mu\mathrm{m}}\left(\mathrm{ergs\ s}^{-1}\right)\right]^{0.8850}. \quad (9)$$

The exponents of equations (8) and (9) are the same within the 3 σ error (the combined 1 σ uncertainty is 0.03). Equation (9) is closer to a linear relation than equation (8) because we add a distance effect when using luminosities (which depend on the distance squared). A large sample of regions with comparable distances may be needed to fully sort out intrinsic effects from distance-related effects. Both relations are derived from best bilinear fitting of data on H II knots, but their extrapolations account for the observed properties of LIRGs as well. In addition, when considering more extended galactic regions or starburst galaxies, equation (8) does not change significantly (Figs. 4 and 8). Equations (8) and (9) may thus be applicable to galaxies in general whose energy output is dominated by recent star formation.

Equation (9) is very similar to that of Alonso-Herrero et al. (2006), who have derived an SFR calibration for the 24 μm luminosity using a sample of ultraluminous infrared galaxies, LIRGs, and NGC 5194. The difference in the calibration constant between our equation (9) and the calibration of Alonso-Herrero et al. (2006) is entirely due to the slight difference in exponent between the two relations and the different SFR-$L(\mathrm{H}\alpha)$ calibrations used here and in that work. Perez-Gonzalez et al. (2006) find a lower exponent, $\sim$0.77, than the one in equation (9), about a 4 σ difference; however, their result is based on line-emitting regions in just two galaxies, NGC 5194 and NGC 3031.

8.3. *The* 8 μm *Emission*

The analysis of the H II knots in M51 has shown a general, nonlinear correlation between the 8 μm and the Paα emission (with exponent 0.79; Calzetti et al. 2005). The present study similarly recovers a nonlinear behavior for the high-metallicity data, albeit less extreme than in the M51 case: $S_{8\ \mu\mathrm{m,dust}} \propto S_{\mathrm{Pa}\alpha\mathrm{,corr}}^{0.94}$. Our simple $Z = Z_{\odot}$ models also predict a nonlinear correlation between the 8 μm and Paα emission, but with an exponent slightly *above* unity. Therefore, the gap between observations and expectations is even wider than a simple deviation from a linear correlation; with our uncertainties, the discrepancy is at the 10 σ level. This level of discrepancy remains unchanged when other uncertainties, e.g., on the dust modeling and on the correlation between dust attenuation and number of ionizing photons (see the Appendix), are included. In contrast, the same simple models are quite successful at explaining the observed trend of $S_{24\ \mu\mathrm{m}}$. We conclude that the 8 μm emission as measured within our apertures must include additional contributions that are not included in our simplified models.

Mechanisms that can produce a lower than expected slope in a correlation between $S_{8\ \mu\mathrm{m,dust}}$ and $S_{\mathrm{Pa}\alpha\mathrm{,corr}}$ include the potential contamination of our measurements by the diffuse emission from the general galactic radiation field (Li & Draine 2002; Haas et al. 2002; Boselli et al. 2004; Peeters et al. 2004; Wu et al. 2005; Mattioda et al. 2005) and/or destruction/fragmentation of the 8 μm emission carriers (Boulanger et al. 1988, 1990; Helou et al. 1991; Houck et al. 2004; Pety et al. 2005). In the case of destruction or fragmentation of the PAH emitters at 8 μm, the brightest H II regions will show a deficiency in the 8 μm luminosity relative to the fainter regions. In the case where nonionizing populations, as well as ionizing ones, heat the 8 μm dust carriers, the contribution of the former to the $S_{8\ \mu\mathrm{m,dust}}$ measurements within our apertures will become proportionally larger as the H II regions become fainter (decreasing $S_{\mathrm{Pa}\alpha\mathrm{,corr}}$), again flattening the observed trend. Finally, if the volume filling factor of the 8 μm luminosity originating in the PDRs evolves differently from that of the H II regions (or other inhomogeneities in the 8 μm emission distribution are present) as the H II region's luminosity increases (Förster Schreiber et al. 2004; Helou et al. 2004), the net result will also be a lower than expected exponent between $S_{8\ \mu\mathrm{m,dust}}$ and $S_{\mathrm{Pa}\alpha\mathrm{,corr}}$.

The correlation exponent predicted by models of the 8 μm LSD versus Paα LSD is better matched by the data of large-scale (multiple kiloparsec) measurements of the centers of the high-metallicity galaxies (Fig. 8). There is, however, an offset between models and observations, in the sense that the data imply about 65%–100% more 8 μm emission than expectations from models. This result argues in favor of one of the mechanisms described above: the presence within our apertures of diffuse 8 μm emission unrelated to the current star formation. Indeed, the result can be explained if stellar populations other than those related to the current star formation can heat the carriers of the 8 μm emission, and their contribution becomes proportionally larger than that of the ionizing populations as the size of the sampled region within each galaxy increases.

The underluminosity of the 8 μm emission at low metallicities (Boselli et al. 2004; Engelbracht et al. 2005; Hogg et al. 2005; Galliano et al. 2005; Rosenberg et al. 2006; Madden et al. 2006; Wu et al. 2006; Draine et al. 2007) is not a function of the intensity of the radiation field (Fig. 6). Metal-poor regions as bright (in ionizing photon density) as metal-rich regions have, nevertheless, 8 μm LSDs that are almost an order of magnitude lower. The most metal-poor regions can be as much as a factor of 30 fainter at 8 μm than their metal-rich counterparts at fixed Paα LSD. In addition to the decrease of the dust opacity with metallicity (the same effect present for the 24 μm), the data require a second ingredient to account for the underluminosity at 8 μm. The second ingredient, from the models of Draine & Li (2007), is the decrease of the mass fraction of the low-mass PAH molecules in the dust mixture for decreasing metallicity. This decrease affects selectively more the 8 μm emission than the 24 μm emission, as the former has a larger fraction of its flux contributed by single-photon excitation of PAHs. The models, indeed, account reasonably well for the observed deficiency of the 8 μm flux in metal-poor objects (Draine et al. 2007). A possible mechanism to reduce the mass fraction of PAH molecules in the low-metallicity galaxies is destruction by the hard radiation field in those galaxies (e.g., Madden et al. 2006; Wu et al. 2006), although these molecules have proven surprisingly robust (Engelbracht et al. 2006). An alternative possibility to destruction is that the lowest metallicity galaxies may not have formed the carriers of the aromatic features in the first place (Engelbracht et al. 2005; Dwek 2005).

The correlation that exists between $\log S_{8\ \mu\mathrm{m,dust}}$ and $\log S_{\mathrm{Pa}\alpha\mathrm{,corr}}$ for the metal-rich regions (eq. [3]) is statistically as significant as those existing for the 24 μm and for the combined optical/MIR luminosity. However, there are many caveats in using such correlation to trace SFRs with the 8 μm emission. First and foremost, stellar populations other than those that are currently forming stars contribute to the MIR emission; thus, a calibration of the 8 μm emission as an SFR tracer will depend on the galactic area probed and, possibly, on the ratio between current and past (or recent past) star formation. A second limitation is the extreme sensitivity of the 8 μm emission to metallicity, which is about an order of magnitude larger than observed for the 24 μm emission.

In all cases, the presence of active galactic nuclei (AGNs) in unresolved galaxies will complicate the use of the MIR band emission for SFR determinations. Galaxies in the SINGS sample that contain central nonthermal sources (Seyfert 2s or LINERs) show prominent nuclear emission in the MIR bands; in our case, the 8 and 24 μm emission from the nonthermal nuclei tends to be

as bright as some of the brightest H II knots in their host galaxies (Figs. 3 and 4).

9. SUMMARY AND CONCLUSIONS

The analysis of the MIR emission, at the *Spitzer* IRAC 8 μm and MIPS 24 μm wavelengths, from a set of local galaxies drawn from the SINGS sample has shown that their viability as SFR indicators is subject to a number of caveats. The calibrations given in this work, provided that the caveats are taken into account, should, however, be useful for measurements of SFRs in actively star-forming galaxies using their observed MIR emission, in the absence of prominent central AGNs.

The most robust of the indicators analyzed in this study is the one proposed by Kennicutt et al. (2007), which combines the observed Hα and 24 μm luminosities as probes of the total number of ionizing photons present in a region. Here we present a calibration (eq. [7]) for that relation that is based on measurements of 220 H II regions/complexes in 33 nearby galaxies. Comparisons with models suggest that the calibration should be applicable to large systems or galaxies whose energy output is dominated by young stellar populations, up to at least LSDs of $S_{\mathrm{Pa}\alpha,\mathrm{corr}} > 10^{40}$–$10^{41}$ ergs s^{-1} kpc^{-2}.

Second best is the 24 μm emission alone, which, although robust (within the limits of our analysis) for metal-rich objects, shows substantial deviations, at the level of factors of 2–4, from the mean trend for decreasing metallicity. Models can account for the observed deviations as an effect of the increased transparency of the medium for lower metal abundances (less dust means less infrared emission). The calibration presented here (eqs. [8] and [9]) is nonlinear and reflects both observations and expectations from models. The calibration is appropriate for metal-rich H II regions or starbursts, and caution should be exercised when applying it to extended star-forming galaxies (R. C. Kennicutt, Jr. & J. Moustakas 2007, in preparation) or to metal-poor targets. In particular, galaxies with a prominent contribution from non-star-forming populations to the integrated light may receive a yet unquantified contribution to the 24 μm emission from a diffuse component. This diffuse component would not be directly related to star formation and may be in the single-photon heating regime; its presence would add to the integrated 24 μm emission and would alter the calibration of this emission for SFR measurements.

We do not present a calibration of the SFR based on the 8 μm emission, as emission at this wavelength shows strong dependence not only on metallicity (more than an order of magnitude) but also on the size (about a factor of 2) and, possibly, star formation history of the region being measured. It should be remarked, however, that when measurements are limited to regions of star formation with a narrow spread in metallicity around the solar value, the 8 μm emission shows a correlation that is almost linear with the ionizing photon rate.

The mean trends between the MIR emission (at 8 μm, 24 μm, and combined optical/MIR) and the ionizing photon tracer Paα are well accounted for by either a 4 Myr old burst of star formation or a >100 Myr old constant star formation model; this provides a measure of the degeneracies in the population models, but also a measure of the general applicability of the calibrations discussed here to both star-forming regions within galaxies and whole star formation–dominated galaxies.

In all cases, the spread around the mean trends has an rms of $\sim$0.3 dex (each side). This spread is well accounted for by allowing stellar populations with a range of ages, between 0 and 8 Myr, to produce the observed emission. The older stellar populations can account for H II knots with high MIR emission relative to the ionizing photon density, although more complex dust geometries than those analyzed here can also contribute to the spread.

Our analysis has concentrated on H II knots and starburst galaxies, where star-forming stellar populations dominate over more evolved populations in the bolometric output of the galaxy. However, the contribution of nonionizing stellar populations to the heating of the dust emitting in the MIR region needs to be fully quantified, in order to test the applicability of (or derive modifications for) the SFR calibrations presented in this work to more general environments, such as quiescently star-forming galaxies. This is the subject of a future investigation that employs the SINGS and other star-forming galaxies as test beds (R. C. Kennicutt, Jr. & J. Moustakas 2007, in preparation).

The authors would like to acknowledge the anonymous referee for the speedy report and for the many constructive comments that have helped improve the manuscript. This work has been partially supported by the NASA *HST* grant GO-9360 and by the JPL, Caltech, contract 1224667. It is part of SINGS, The Spitzer Infrared Nearby Galaxies Survey, one of the *Spitzer Space Telescope* Legacy Science Programs. This work has made use of the NASA/IPAC Extragalactic Database (NED), which is operated by the Jet Propulsion Laboratory, California Institute of Technology, under contract with the National Aeronautics and Space Administration.

APPENDIX

MODELS OF DUST ABSORPTION AND EMISSION

A1. THE ENERGY BALANCE

To aid the interpretation of the observed correlations between the MIR emission and the Paα emission (a tracer of the number of ionizing photons), we build a simple model of dust attenuation of the SED of young stellar populations at UV to near-IR wavelengths, with the prescription that the dust-absorbed energy is reemitted in the MIR/far-IR with an SED that follows the Draine & Li (2007) models. Ideally, the "perfect" estimator of SFR should correlate linearly with the SFR itself. We have seen in § 6 that this is not the case for $S_{24\ \mu\mathrm{m}}$ and $S_{8\ \mu\mathrm{m,dust}}$; a legitimate question is whether the nature of the observed nonlinearity is such to jeopardize a reliable use of the MIR emission as an SFR indicator. Thus, our main interest in this section is to understand whether a heuristic model can account for the observed trends as a function of both LSD and metallicity and is able to (1) reproduce the observed MIR emission level and its trend as a function of the Paα LSD with simple prescriptions for the stellar emission spectrum, dust geometry, and ISM metallicity in the regions; (2) provide a physical explanation for the nonlinear correlations between the MIR LSDs and the line emission LSD; and (3) match overall expectations on the age of the stellar populations in the H II knots.

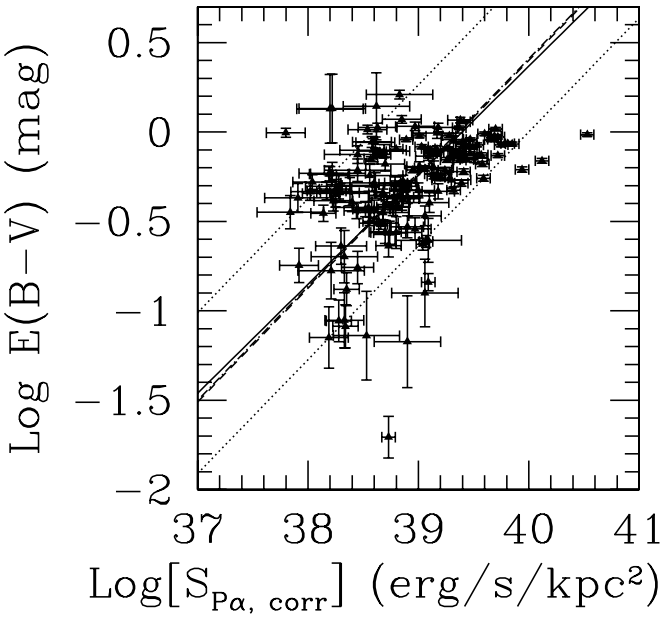

FIG. 12.—Color excess $E(B-V)$, measured from the Hα/Paα ratio (§ 3.2), as a function of the Paα LSD, for the 164 H II knots in the high-metallicity subsample. The best bilinear fit through the data (*solid line*) has slope 0.61 (eq. [A2]). The dotted lines mark the region containing 90% of the data points around the best-fit line. The dashed line is from eq. (A3), where the slope is kept at the fixed value 0.64 (from the Schmidt law in NGC 5194; Kennicutt et al. 2007).

For the simplest assumption that the dust extinction is described as an effective foreground attenuation $A(\lambda)$ (Calzetti et al. 1994; Meurer et al. 1999), the bolometric (3–1000 μm) infrared luminosity $L_{\rm IR}$ is given by

$$L_{\rm IR} = \int_0^\infty F_S(\lambda)\left[1 - 10^{-0.4A(\lambda)}\right] d\lambda, \tag{A1}$$

where $F_S(\lambda)$ is the stellar light SED. We use the "foreground attenuation" as a working hypothesis, since it enables us to account for both absorption and scattering (in and out of the line of sight) of the stellar light by dust with a simple expression (Calzetti et al. 1994, 2000). Potential limitations to this assumption are discussed in § A4.

Our general results indicate a correlation between the MIR emission and the number of ionizing photons in H II knots. Similar correlations have been observed for whole galaxies (e.g., Roussel et al. 2001; Förster Schreiber et al. 2004; Wu et al. 2005; Alonso-Herrero et al. 2006) and are qualitatively not dissimilar from the correlation between the bolometric infrared emission and the SFR derived for galaxies dominated by young stellar populations using *IRAS* data (Lonsdale Persson & Helou 1987; Rowan-Robinson & Crawford 1989; Devereux & Young 1990; Sauvage & Thuan 1992). Equation (A1) shows that such correlations are mediated by the dust attenuation $A(\lambda)$; indeed, starburst and star-forming galaxies have been shown to be redder and to suffer generally higher dust attenuation as their SFRs increase (Wang & Heckman 1996; Heckman et al. 1998; Hopkins et al. 2001; Calzetti 2001; Moustakas et al. 2006). This general trend is also shown by the H II knots in our sample. A plot of the color excess $E(B-V)$,[24] derived from the Hα/Paα ratios of individual H II knots, as a function of the Paα LSD is shown in Figure 12, together with the best fit through the data points. The data in Figure 12 are for the high-metallicity subsample, the group with the largest number of data points and the widest range in color excess in our sample. If we introduce the ionizing photon rate per unit area, $\Sigma_{\rm ion}$, in units of s^{-1} kpc^{-2} as derived directly from $S_{\rm Pa\alpha,corr}$ for case B recombination, then in solar metallicity regions $E(B-V)$ is related to the ionizing photon rate via the best fit (bilinear on the log of the quantities):

$$E(B-V) = 0.21\left(\frac{\Sigma_{\rm ion}}{10^{51}\ {\rm s^{-1}\ kpc^{-2}}}\right)^{(0.61\pm0.03)}, \tag{A2}$$

where $E(B-V)$ is in magnitudes. The correlation has 5.7 σ significance and is independent of the specifics of the stellar population (age, burst or constant star formation, etc.).

Some physical insights on the meaning of equation (A2) can be gained by looking at the implications of the scaling laws of star formation. The Schmidt law (Kennicutt et al. 1989; Kennicutt 1998b) provides a way to relate the SFR density to the gas density in galaxies. Furthermore, in our own Galaxy, there is a tight correlation between the color excess $E(B-V)$ and the gas (H I+H_2) column density (Bohlin et al. 1978). By combining the Schmidt law, as derived locally for regions in NGC 5194 (Kennicutt et al. 2007), and the extinction–gas column density correlation, we get a relation between the color excess and the SFR density:

$$E(B-V) = 10.30\gamma\Sigma_{\rm SFR}^{0.64}, \tag{A3}$$

[24] $A(\lambda) = k(\lambda)E(B-V)$, where $k(\lambda)$ is the extinction curve (§ 3.2).

where $\Sigma_{\rm SFR}$ is in units of $M_\odot$ yr^{-1} kpc^{-2} and the factor γ accounts for the fact that not all the gas (and the dust) is in front of the stars. Equation (A3) can be readily related to equation (A2), since the two exponents, 0.61 in the first and 0.64 in the second equation, are formally the same number within the 1 σ uncertainty of our fitting procedure (see also Fig. 12). By fitting the data of Figure 12 with a straight line of fixed slope 0.64 (eq. [A3]), we get an estimate of $\gamma = 0.4$–0.45 for the constant star formation models, depending on the time elapsed since the onset of star formation (6–100 Myr). This value of γ is very close to the mean value of 0.5 expected in the case in which the star formation is located on average at the midpoint of the gas column density.

Metallicity variations in the stellar populations produce small variations in equation (A2). However, observations of the extinction–to–gas column density correlation for the Large and Small Magellanic Clouds suggest roughly linear scaling with metallicity (Koorneef & Code 1981; Bouchet et al. 1985). This is likely to be the dominant dependence of equation (A2) on metallicity, and we model it as a linear dependence on Z, the ISM's metallicity in solar units:

$$E(B-V) = 0.21Z\left(\frac{\Sigma_{\rm ion}}{10^{51}\ {\rm s^{-1}\ kpc^{-2}}}\right)^{0.61}. \tag{A4}$$

Although nonparametric (Spearman and Kendall) rank tests indicate that the data in Figure 12 deviate from the null (uncorrelated) hypothesis by 5.7 σ, the spread around the mean trend is still significant. The 90% boundary is located at (−0.4 dex, +0.5 dex) along the vertical axis. We see in § A4 that the large spread in Figure 12 has a small impact on the main conclusions of this appendix. That said, it should be important to keep in mind that although the trends have a physical base in the combination of the Schmidt law with the extinction–gas column density correlation (T. M. Heckman 2004, private communication; C. A. Tremonti 2006, private communication), individual variations remain important.

Equations (A2) and (A4) are used in combination with equation (A1) in the following sections to provide a heuristic description of the relation between ionizing photon rates (SFRs) and monochromatic dust emission in our regions, in order to understand the broad trends observed in the data. Thus, equations (A2) and (A4) are derived from data and are used to explain data, and the potential of circular argument should be addressed. The data in Figure 12 are completely independent of the data presented in Figures 3, 4, and 7. The color excess $E(B-V)$ is derived from ionized gas emission, while the monochromatic dust emission is mainly due to stellar continuum emission. Equation (A1) also requires independent assumptions on the underlying stellar population and the dust geometry relative to both the stellar population and the ionized gas (see next section and Calzetti et al. 1994). Therefore, the use of the extinction–ionizing photon correlation of equations (A2) and (A4) is unlikely to automatically enforce a fit to the data in Figures 3, 4, and 7. Finally, we see in § A4 that equations (A2) and (A4) are not necessary to account for the observed data for Paα LSDs above $\sim 3\times10^{38}$ ergs s^{-1} kpc^{-2}.

A2. MODEL PARAMETERS

For $F_S(\lambda)$ in equation (A1), we adopt the stellar population models of Starburst99 (2005 update; Leitherer et al. 1999). Since we are exploring the infrared emission of both H II knots and star formation–dominated galaxies, we consider both bursts of star formation and constant star formation. Burst models are explored in the age range 0–10 Myr, as older ages do not produce enough ionizing photons to provide Paα-detectable H II knots in our data. As bursts age, the number of ionizing photons produced by the massive, short-lived stars decreases, while the UV–optical stellar luminosity (the main contributor to the infrared emission) remains comparatively high, since it is contributed by lower mass, longer living stars. Thus, aging stellar populations produce high-luminosity ratios $L({\rm IR})/L({\rm Pa}\alpha)$. For constant star formation, the representative case of a 100 Myr duration model is considered. The difference between this model and a much younger case is the increase of optical and infrared light in the older model, due to the accumulation of previous-generation, low-mass, long-lived stars. The light from these older stars contributes to $L({\rm IR})$, but not to the ionizing photon budget. The net effect is that the 100 Myr constant star formation model produces about twice as much infrared emission as a, e.g., 6 Myr old case, for the same dust opacity. The variation between the 100 Myr and 1 Gyr models is about 6%. For the stellar IMF, we adopt the Starburst99 default, which consists of two power laws, with slope −1.3 in the range 0.1–0.5 $M_\odot$ and slope −2.3 in the range 0.5–120 $M_\odot$. The SFRs derived from this IMF are a factor of 1.59 smaller than those derived from a Salpeter IMF in the range 0.1–100 $M_\odot$, for the same number of ionizing photons.

For the wavelength dependence of the dust attenuation in equation (A1), $A(\lambda) = k(\lambda)E(B-V)$, we adopt the starburst obscuration curve of Calzetti (2001) (see also Calzetti et al. 1994, 2000; Meurer et al. 1999), which prescribes an attenuation of the stellar continuum a factor of 0.44 that of the emission lines.

The fraction of the infrared luminosity that emerges in the IRAC 8 μm and MIPS 24 μm bands, $L(8)/L({\rm IR})$ and $L(24)/L({\rm IR})$, is from the model of Draine & Li (2007), which updates the model of Li & Draine (2001). At solar metallicity, the two papers provide consistent prescriptions for our case. The fraction of infrared light emitted in either the 8 or 24 μm band increases nonlinearly as a function of the starlight intensity (Fig. 15 of Draine & Li 2007); the ratios are flat at the low-intensity end (single-photon heating of dust) and rise sharply at higher intensities, producing "hotter" infrared SEDs, i.e., peaked at shorter wavelengths. At solar metallicity, the dependence of $L(8)/L({\rm IR})$ as a function of the starlight intensity is much shallower than that of $L(24)/L({\rm IR})$; the former varies by 50% over the full range of intensities analyzed here, while the latter changes by more than a factor of 10. The results of Draine & Li (2007) are expressed as a function of the parameter U, the starlight intensity in units of the solar neighborhood value.

We relate the typical stellar radiation field in our H II knots to U using the individual H II regions detected in the *HST* Paα image of the nearby (and thus better resolved), actively star-forming galaxy NGC 6946. From the image we measure the sizes, defined as the radius of the circular area containing 80% of the Paα emission in each region, and line emission values of the H II regions. Total luminous energies are derived by associating the range of stellar models described above to the measured line intensities, and energy densities are derived by dividing for the measured volumes. By extrapolating the observed quantities, we find that burst models

with mass $10^6\ M_\odot$ and ages <6 Myr or constant star formation models with SFR $= 1\ M_\odot\ \mathrm{yr}^{-1}$ ($L_{\mathrm{Pa}\alpha,\mathrm{corr}} \lesssim 10^{40}$ ergs s^{-1}), with radii $R \approx 100$ pc, produce average starlight intensities $U \sim 400$–1200. The factor of $\sim$3 variation in U accounts for two uncertainties in our derivation: (1) star-forming regions have hotter SEDs than the local ISM (Mathis et al. 1983), and (2) our stellar models and regions' sizes cover a range of values/characteristics. The presence of dust absorption within the H II region and the conversion of some of the energy to free-free emission also contribute to the uncertainty (and some decrease) in U. However, the results described in the next section are fairly insensitive to the actual value of U, within the range of 3–4 uncertainty detailed above. The relation between number of ionizing photons and starlight intensity derived above suggests that, for constant radii of the H II regions, the transition from single-photon heating to thermal equilibrium heating for the 24 μm emission begins to occur at emission-line intensities $S_{\mathrm{Pa}\alpha,\mathrm{corr}} \approx 10^{39}$ ergs s^{-1} kpc^{-2}.

The impact of metallicity variations is explored by considering how the infrared emission changes under the two conditions that the regions/galaxies have solar metallicity ($Z = Z_\odot$) and 1/10 solar metallicity ($Z = 1/10\ Z_\odot$). The latter value is at the low end of the metallicity range in our sample; our goal is, indeed, to model the lower envelope to the data. The metallicity enters in two components of equation (A1). The first component is the stellar population model, for which we use two metallicity values: solar and $\frac{1}{5}$ solar (Starburst99 does not provide models for our default $1/10\ Z_\odot$, and $\frac{1}{5}\ Z_\odot$ is the closest metallicity value for the stellar populations). The second component is the dependence of the color excess on metallicity, which we describe in a linear fashion via equation (A4). Additional metallicity-dependent ingredients are the conversion from ionizing photon rate to hydrogen nebular line luminosity (at the $\sim$15% level; see § 3.2) and the fraction of infrared light emerging in the 8 and 24 μm bands. We use, again, the model of Draine & Li (2007) for the latter, with the assumption that variable metallicities have a major impact on the mass fraction of the PAHs in the dust mixture;[25] this, in turn, affects the dust emission in the MIR bands, mainly the IRAC 8 μm band, which results predominantly from single-photon heating at low values of the starlight intensity. For reference, in the low-U regime, $L(24)/L(\mathrm{IR})$ changes by about 60% and $L(8)/L(\mathrm{IR})$ changes by an order of magnitude for a factor of 10 variation in the abundance of small PAH; the differences become negligible at the high-U end (Draine & Li 2007).

A3. GENERAL MODEL TRENDS

In the extreme case that we have no dust in our region, equation (A1) will be null, and there will be no relation between SFR (or ionizing photon rate) and dust emission. In the presence of even small amounts of dust, however, the relation established by equation (A1) will produce a general trend, with details that depend on a host of parameter assumptions. At the lowest levels of dust extinction, the relation between $L(\mathrm{IR})$ and the number of ionizing photons is nonlinear, with an asymptotic exponent of 1.64 for our equations (A1)–(A4); a linear relation is established only once the integral on the right-hand side of equation (A1) corresponds to most of the stellar energy. In other words, once the region contains enough dust that most of the stellar energy is absorbed and reemitted in the IR, larger numbers of ionizing photons will linearly correspond to larger IR luminosities.

The impact of the stellar population parameters on the characteristics of the 8 and 24 μm emission has already been shown in Figures 9–11. Stellar populations undergoing constant star formation since 100 Myr in the range SFR $= 4 \times 10^{-5}$ to $4\ M_\odot\ \mathrm{yr}^{-1}$ have equivalent characteristics to bursts of star formation of constant age 4 Myr and mass in the range $M = 10^3$–$10^8\ M_\odot$. For the burst models, the impact of age variation is investigated at constant cluster mass ($10^6\ M_\odot$) and in the two cases of constant or age-variable (eq. [A2]) color excess. The general effect of increasing the age is to move the model curves toward smaller values of the ionizing photon rates for roughly constant IR emission, almost independently of assumptions on the variation (or constancy) of the color excess.

The introduction of the age-variable extinction (via eq. [A2]), however, attempts to mimic the observation that aging H II regions tend to be less dust extincted than the younger H II regions, whether because the more evolved populations have shed the native cocoon or have migrated away from it through secular motions (Mayya & Prabhu 1996). This also introduces a modest dependence of the IR SED and the fraction of infrared light emerging in the 8 and 24 μm bands on age, via changes in the starlight intensity that aging H II regions produce. However, the model does not include additional effects, such as the expansion of H II regions as they evolve, that will affect the IR SED via the decrease of the dust temperature.

Not surprisingly, metallicity variations have a strong effect on the observed MIR emission as a function of the number of ionizing photons (Fig. 13). For the 24 μm emission, most of the effect comes from the fact that the ISM is more transparent at lower metallicities. For the 8 μm emission, roughly equal contributions are given by the more transparent medium and by the decreased mass fraction of low-mass PAH molecules in the dust mixture (Fig. 13, *left panel*).

The fiducial model for the IR SED as a function of starlight intensity (from Draine & Li 2007) is compared with the more extreme assumption that the IR SED is constant for all analyzed regions/galaxies. For the assumption $L(24\ \mu\mathrm{m})/L(\mathrm{IR}) = \mathrm{const} = 0.3$ (Fig. 13, *right panel*), the model line has a different curvature from our fiducial one, starting with higher $\log S_{24\ \mu\mathrm{m}}$ values at low Paα LSD, overshooting the data points in the LSD range $\log S_{\mathrm{Pa}\alpha,\mathrm{corr}} = 39$–$40$, and converging to a slope of unity at higher LSD values. Our fiducial model appears to better reproduce the slope of $\sim$1.23 of the best fit to the data points (in the log-log diagram), and this slope is entirely due to the relation between $L(24)/L(\mathrm{IR})$ and the starlight intensity. For the $L(8)/L(\mathrm{IR})$ ratio, the change between a constant IR SED and a starlight intensity–dependent SED is small, as the ratio changes by about 50% in the full range of LSD under consideration in this work.

A4. MODEL UNCERTAINTIES AND LIMITATIONS

The simple assumptions on stellar populations and dust geometry made in the previous section lead to a number of limitations. Furthermore, the data show in some cases (e.g., Fig. 12) significant dispersion around the mean trend. The impact of considering different assumptions or including the full range (90th percentile) of data dispersion is briefly discussed here.

[25] Based on Draine et al. (2007), a factor of 9–10 difference in the mass fraction of small PAH is a reasonable assumption for metallicities between $Z \sim 0.1$ and $Z > 0.5$.

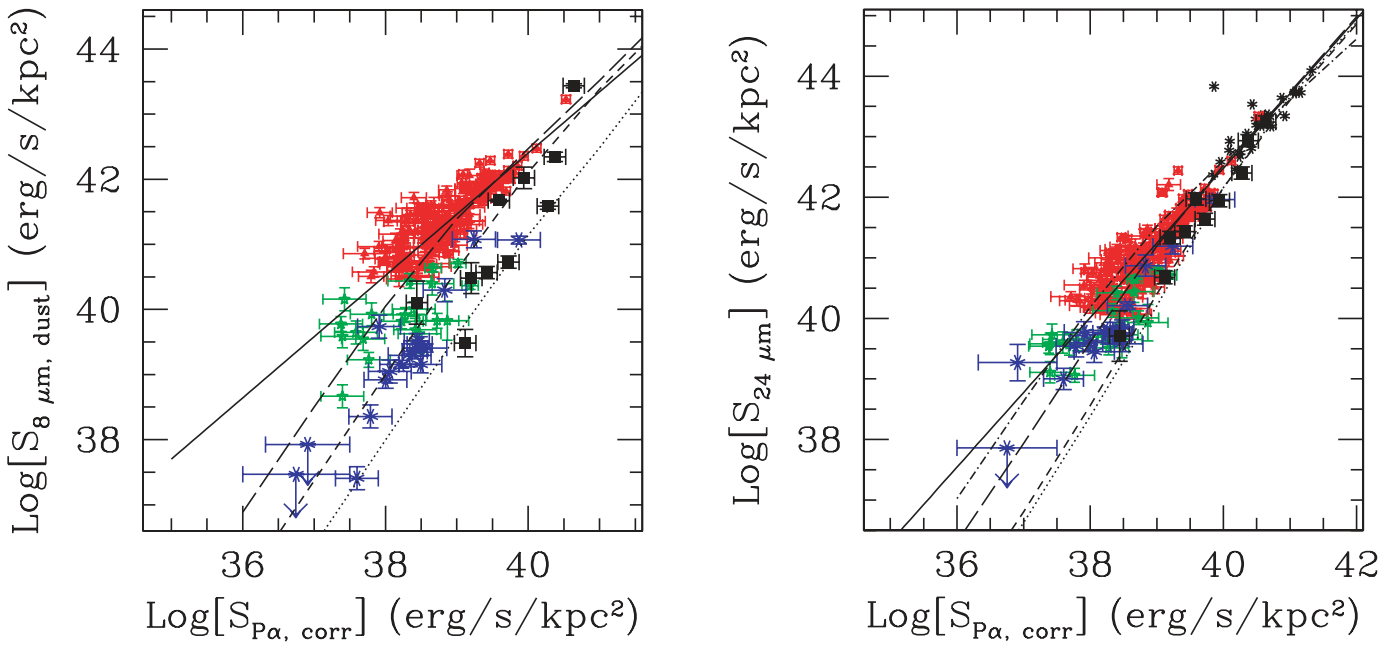

FIG. 13.—Models of dust absorption and emission for constant star formation populations and variable metallicity compared with data, for the 8 μm (*left*) and the 24 μm (*right*) LSD as a function of the Paα LSD. Symbols for the H II knots, the local starbursts, and the LIRGs are as in Figs. 9 and 10. Straight solid lines are the best fits through the high-metallicity H II knots, similar to the lines in Figs. 3 and 4. All models are for a 100 Myr old constant star formation population and include solar metallicity ($Z = Z_\odot$; *long-dashed line*), 1/10 $Z_\odot$ and standard low-mass PAH molecule fraction (*short-dashed line*), and 1/10 $Z_\odot$ and depleted low-mass PAH molecule fraction (*dotted line*; Draine & Li 2007). For the 24 μm vs. Paα plot, the effects of variations in the IR SED are also explored; in particular, our default assumption for the shape of the IR SED as a function of the starlight intensity (Draine & Li 2007) is compared with the extreme assumption that the IR SED is constant, i.e., $L(24)/L(\mathrm{IR}) = \mathrm{const} = 0.3$ (*dot-dashed line*).

The 90th percentile region for the $E(B-V)$ versus Paα LSD correlation is shown in Figure 12 by dotted lines that enclose 90% of the data around the mean correlation. The same region is reproduced on the 24 μm versus Paα LSDs in Figure 14 (*left panel*). We do not show the case for the 8 μm LSD because the results are similar for both MIR bands. The dispersion in the color excess for fixed Paα LSD has a minor impact on our baseline conclusions for the MIR emission, with significant impact (factor of $\sim$6 peak-to-peak variation) concentrated toward the low-intensity, and low-extinction, regions. This effect is readily understood by recalling that once

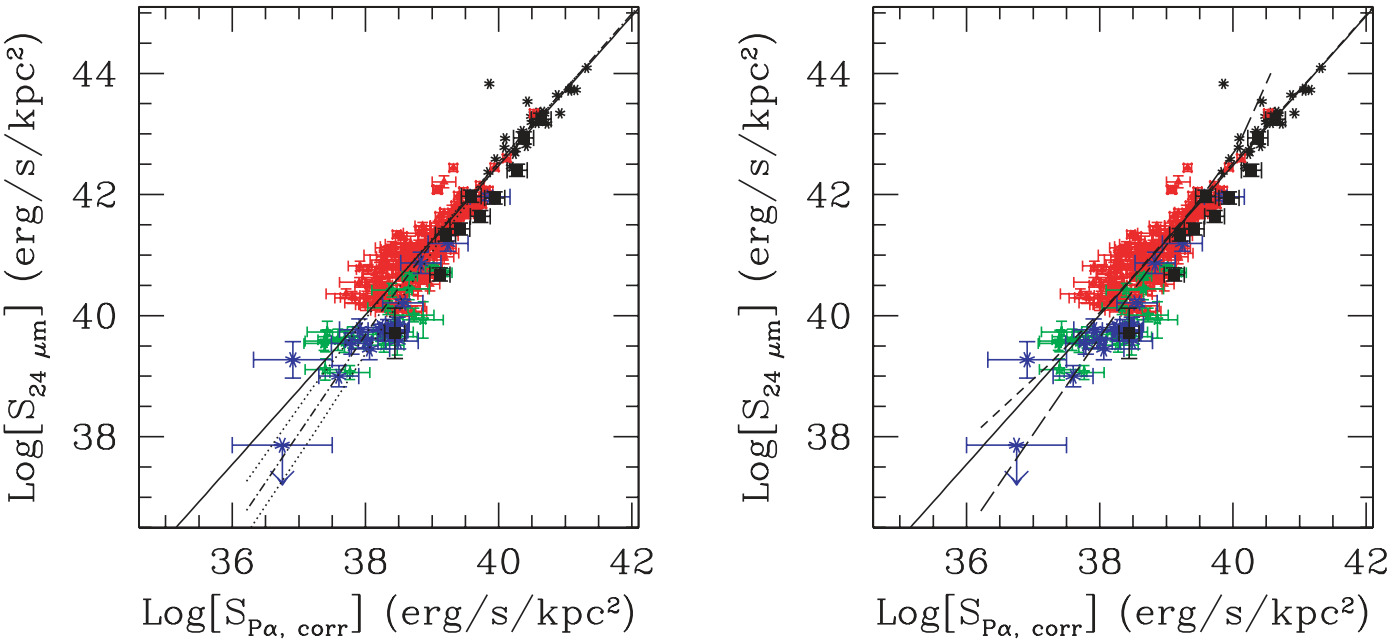

FIG. 14.—The 24 μm LSD as a function of Paα, together with the best-fit line (*straight solid line*, Fig. 4). *Left*: Fiducial model of a dusty 4 Myr old stellar cluster with increasing mass (*dot-dashed line*) is bracketed by the dispersion curves derived from including in eq. (A1) the 90th percentile region of the $E(B-V)$ vs. $S_{\mathrm{Pa}\alpha,\mathrm{corr}}$ correlation (*dotted lines*; Fig. 12). *Right*: Model lines for a 4 Myr old stellar cluster of increasing mass, and two assumptions for the dust distribution that are different from our baseline model: (1) foreground dust geometry and constant $E(B-V) = 1$ as a function of $S_{\mathrm{Pa}\alpha,\mathrm{corr}}$ (*short-dashed line*), and (2) a homogeneously mixed dust-star geometry with no differential extinction between gas and stars, and variable $E(B-V)$ according to eq. (A2) (*long-dashed line*).

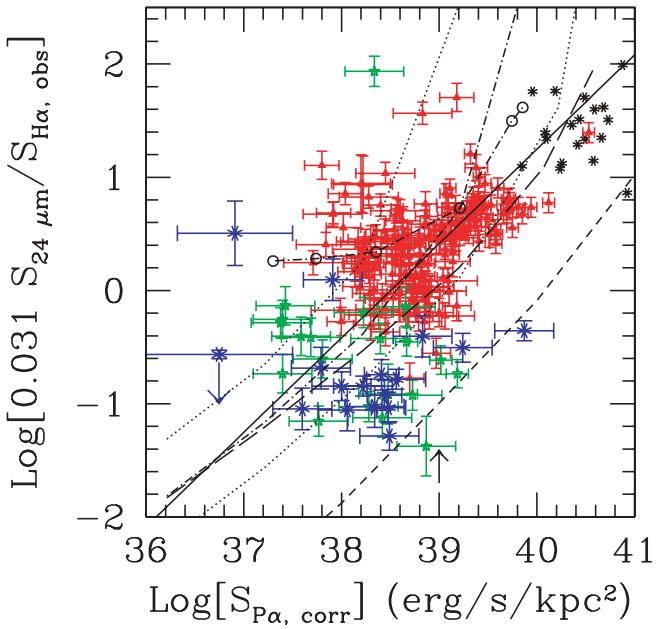

FIG. 15.—Ratio of the 24 μm to the observed Hα LSD as a function of Paα, for the H II knots and LIRGs (Fig. 9), compared with models. The data points are correlated with a $\sim$7 σ significance; the solid line is the best bilinear fit through the data and has slope 0.83. Solar metallicity models include the following (Fig. 9): instantaneous burst with variable mass (10^3–$10^8\,M_\odot$) and color excess and constant age of 4 Myr (*dot-dashed line*); instantaneous burst with constant mass ($10^6\,M_\odot$), variable age, and variable color excess (*dot-dashed line with open circles*, marking, right to left, 0.01, 2, 4, 6, 8, and 10 Myr). The dotted lines mark the upper and lower boundaries to the 90th percentile region from Fig. 12. The long-dashed line is the model of homogeneous dust-stars mixture, with no differential extinction between gas and stars, from Fig. 14. The short-dashed line is the 1/10 solar metallicity model and marks the lower envelope to the data points. The upward-pointing arrow marks the approximate luminosity where the transition between single-photon heating and thermal equilibrium heating for the dust begins to occur (Fig. 9).

the color excess $E(B-V) > 0.5$ mag, over 90% of the UV emission is converted by dust into IR emission. Thus, the dependence of $E(B-V)$ on the Paα LSD for $S_{\mathrm{Pa}\alpha,\mathrm{corr}} \gtrsim 10^{39}$ ergs s^{-1} kpc^{-2} has little impact on the amount of IR emission produced for stellar SEDs that emit most of their power in the UV.

The independence of the IR luminosity on the color excess for high Paα LSDs is also shown for the case where $E(B-V)$ is independent of $S_{\mathrm{Pa}\alpha,\mathrm{corr}}$ (i.e., eqs. [A2]–[A4] are not applied). As a simplified example of $E(B-V)$ independent of $S_{\mathrm{Pa}\alpha,\mathrm{corr}}$, Figure 14 (*right panel*) shows the case of constant value $E(B-V) = 1$ for all Paα LSDs. As long as the color excess is sufficiently large that most of the UV stellar light is attenuated by dust, the model's trend for high-luminosity regions does not change. However, when extended to low LSDs, the model with constant $E(B-V)$ tends to exceed the low-metallicity data points and to show a flatter slope than the best-fit line through the high-metallicity data. The latter is due to the models having reached the single-photon heating for the 24 μm emission, where there is a linear correlation between $S_{24\,\mu\mathrm{m}}$ and $S_{\mathrm{Pa}\alpha,\mathrm{corr}}$.

Age variations among different regions have been discussed in § 7, and they effectively account for the spread around the mean trend for the infrared versus Paα LSDs (Figs. 9–11). Here we discuss the effect of adopting different dust models than our default one.

Most nonforeground dust geometries, e.g., mixtures of dust and gas/stars, will have the effect of "hiding" from direct detection a proportionally larger fraction of the stellar emission than foreground geometries, thus increasing the observed infrared emission, as well as $S_{24\,\mu\mathrm{m}}$ and $S_{8\,\mu\mathrm{m,dust}}$, relative to the ionizing photon rate ($S_{\mathrm{Pa}\alpha,\mathrm{corr}}$) that can be recovered with simple extinction correction methods (e.g., from Hα/Paα). Figure 14 (*right panel*) shows the effect of replacing our foreground dust assumption with a homogeneously mixed dust/stars geometry. The new model follows closely our baseline model up to LSDs $S_{\mathrm{Pa}\alpha,\mathrm{corr}} \sim 3 \times 10^{39}$ ergs s^{-1} kpc^{-2} and deviates upward of the baseline model for higher LSDs. This is the regime where the dust opacity is such that our standard procedure does not recover completely the number of ionizing photons and $S_{\mathrm{Pa}\alpha,\mathrm{corr}}$ is underestimated. If we were to allow for dusty cores with arbitrarily high attenuation values in our H II knots, the mixed model would deviate from the baseline model at arbitrarily low Paα LSDs, thus at least partially accounting for the dispersion of the data points around the mean trend.

The competition of the dust with the gas for absorption of the ionizing photons will become increasingly more effective as the density of the star-forming regions increases, as in the case of LIRGs and brighter infrared galaxies. Rigby & Rieke (2004) propose that the lack of high-excitation infrared fine-structure lines in infrared galaxies is due to much of the massive star formation occurring in ultracompact H II regions, where such competition would be significant. Dopita et al. (2006) have modeled the behavior of such regions, confirming that the infrared continuum should get warmer, but also show the potential to suppress the emission lines substantially.

One of the main assumptions in our analysis is that the "typical" H II knot in our sample is described by a single mean stellar population. Realistically, variations are expected, not only from galaxy to galaxy, but also from region to region. Under most circumstances, each of our apertures will include multiple stellar populations covering a range of ages (Calzetti et al. 2005). Furthermore, the dust covering factor may change from population to population within each region, with older stellar populations often located in areas of lower extinction, or located farther away from the dust they heat. The ratio of the 24 μm LSD to the observed Hα LSD, which by construction exacerbates any effect of dust extinction (Fig. 15), can provide insights into this effect. The ratio 24 μm/Hα_{obs} spans more than 2 orders of magnitude for our data, with values between $\sim$0.04 and $\sim$10. The $S_{24\,\mu\mathrm{m}}/S_{\mathrm{H}\alpha,\mathrm{obs}}$ ratio is correlated (with a 7 σ significance for

a Spearman nonparametric test) with the Paα LSD, with slope 0.83 ± 0.03 in a log-log plane. This is a different way of expressing the correlation between star formation and dust extinction already shown in Figure 12.

The model lines for solar metallicity are within the general locus of the data points at low values of the Paα LSD, especially when the 90th percentile region from Figure 12 is included (Fig. 15). The brightest regions in Paα LSD, as well as most of the LIRGs, tend to be more consistent with a model where stars and dust are homogeneously mixed and there is no differential extinction between gas and stars (as assumed in all our baseline models, from Calzetti et al. 1994). This is not unexpected, as strongly star-forming regions are in general more heavily enshrouded in dust than less active regions (Goldader et al. 2002). In addition, in this regime, small errors in the measurement of the (faint) Hα line can produce large deviations of the data. The moderate discrepancy between the baseline models and data at the high-luminosity end seen in Figure 15 has negligible impact on our results for the MIR LSDs as a function of the Paα LSD (§ 6): in this regime, over 80% of the UV light is reprocessed by dust into the infrared, and large fluctuations on the stellar light observed directly (including the nebular hydrogen lines) produce only small changes of L(IR).

Despite the potential shortcomings of our assumptions, the ability of the models to describe the overall trends of the data enables us to dissect the individual "ingredients" that produce the observed correlations to better understand their origin.

REFERENCES

Allamandola, L. J., Tielens, A. G. G. M., & Barker, J. R. 1985, ApJ, 290, L25
Allende Prieto, C., Lambert, D. L., & Asplund, M. 2001, ApJ, 556, L63
Alonso-Herrero, A., Rieke, G. H., Rieke, M. J., Colina, L., Perez-Gonzalez, P. G., & Ryder, S. D. 2006, ApJ, 650, 835
Barger, A. J., Cowie, L. L., Sanders, D. B., Fulton, E., Taniguchi, Y., Sato, Y., Kawara, K., & Okuda, H. 1998, Nature, 394, 248
Barker, E., et al. 2006, The Near Infrared Camera and Multi-Object Spectrometer Instrument Handbook, Version 9.0 (Baltimore: STScI)
Bell, E. F. 2003, ApJ, 586, 794
Bendo, G. J., et al. 2006, ApJ, 652, 283
Bohlin, R. C., Savage, B. D., & Drake, J. F. 1978, ApJ, 224, 132
Böker, T., et al. 1999, ApJS, 124, 95
Boselli, A., Lequeux, J., & Gavazzi, G. 2004, A&A, 428, 409
Bouchet, P., Lequeux, J., Maurice, E., Prevot, L., & Prevot-Burnichon, M. L. 1985, A&A, 149, 330
Boulanger, F., Beichmann, C., Desert, F.-X., Helou, G., Perault, M., & Ryter, C. 1988, ApJ, 332, 328
Boulanger, F., Falgarone, E., Puget, J. L., & Helou, G. 1990, ApJ, 364, 136
Buat, V., Boselli, A., Gavazzi, G., & Bonfanti, C. 2002, A&A, 383, 801
Buat, V., et al. 2005, ApJ, 619, L51
Calzetti, D. 2001, PASP, 113, 1449
Calzetti, D., Armus, L., Bohlin, R. C., Kinney, A. L., Koornneef, J., & Storchi-Bergmann, T. 2000, ApJ, 533, 682
Calzetti, D., Kinney, A. L., & Storchi-Bergmann, T. 1994, ApJ, 429, 582
Calzetti, D., et al. 2005, ApJ, 633, 871
Chapman, S. C., Blain, A. W., Smail, I., & Ivison, R. J. 2005, ApJ, 622, 772
Daddi, E., et al. 2005, ApJ, 631, L13
Dale, D. A., Helou, G., Contursi, A., Silbermann, N. A., & Kolhatkar, S. 2001, ApJ, 549, 215
Dale, D. A., et al. 2007, ApJ, 655, 863
de Vaucouleurs, G., de Vaucouleurs, A., Corwin, H. G., Jr., Buta, R. J., Paturel, G., & Fouque, P. 1991, Third Reference Catalogue of Bright Galaxies, Version 3.9 (Berlin: Springer)
Devereux, N. A., & Young, J. S. 1990, ApJ, 350, L25
Dopita, M. A., et al. 2006, ApJ, 639, 788
Draine, B. T., & Li, A. 2007, ApJ, 657, 810
Draine, B. T., et al. 2007, ApJ, 663, 866
Dwek, E. 2005, in AIP Conf. Proc. 761, The Spectral Energy Distributions of Gas-rich Galaxies: Confronting Models with Data, ed. C. C. Popescu & R. J. Tuffs (New York: AIP), 103
Eales, S., Lilly, S., Gear, W., Dunne, L., Bond, J. R., Hammer, F., Le Fevre, O., & Crampton, D. 1999, ApJ, 515, 518
Engelbracht, C. W., Gordon, K. D., Rieke, G. H., Werner, M. W., Dale, D. A., & Latter, W. B. 2005, ApJ, 628, L29
Engelbracht, C. W., et al. 2006, ApJ, 642, L127
———. 2007, PASP, in press (arXiv: 0704.2195v1)
Fang, F., et al. 2004, ApJS, 154, 35
Fitzpatrick, E. L. 1986, AJ, 92, 1068
Förster Schreiber, N. M., Roussel, H., Sauvage, M., & Charmandaris, V. 2004, A&A, 419, 501
Galliano, F., Madden, S. C., Jones, A. P., Wilson, C. D., & Bernard, J.-P. 2005, A&A, 434, 867
Garnett, D. R., Kennicutt, R. C., Jr., & Bresolin, F. 2004, ApJ, 607, L21
Goldader, J. D., Meurer, G., Heckman, T. M., Seibert, M., Sanders, D. B., Calzetti, D., & Steidel, C. C. 2002, ApJ, 568, 651
Gordon, K. D., et al. 2005, PASP, 117, 503
Haas, M., Klaas, U., & Bianchi, S. 2002, A&A, 385, L23
Heckman, T. M., Robert, C., Leitherer, C., Garnett, D. R., & van der Rydt, F. 1998, ApJ, 503, 646
Helfer, T. T., Thornley, M. D., Regan, M. W., Wong, T., Sheth, K., Vogel, S. N., Blitz, L., & Bock, D. C.-J. 2003, ApJS, 145, 259
Helou, G. 1986, ApJ, 311, L33
Helou, G., Khan, I. R., Malek, L., & Boehmer, L. 1988, ApJS, 68, 151
Helou, G., Ryter, C., & Soifer, B. T. 1991, ApJ, 376, 505
Helou, G., et al. 2004, ApJS, 154, 253
Ho, L. C., Filippenko, A. V., & Sargent, W. L. W. 1997, ApJS, 112, 315
Hogg, D. W., Tremonti, C. A., Blanton, M. R., Finkbeiner, D. P., Padmanabhan, N., Quintero, A. D., Schlegel, D., & Wherry, N. 2005, ApJ, 624, 162
Hoopes, C. G., & Walterbos, R. A. M. 2003, ApJ, 586, 902
Hopkins, A. M. 2004, ApJ, 615, 209
Hopkins, A. M., Connolly, A. J., Haarsma, D. B., & Cram, L. E. 2001, AJ, 122, 288
Houck, J. R., et al. 2004, ApJS, 154, 211
Hughes, D. H., et al. 1998, Nature, 394, 241
Jarrett, T. 2006, IRAC Extended Source Calibration (Pasadena: Caltech)
Kennicutt, R. C., Jr. 1998a, ApJ, 498, 541
———. 1998b, ARA&A, 36, 189
Kennicutt, R. C., Jr., Edgar, B. K., & Hodge, P. W. 1989, ApJ, 337, 761
Kennicutt, R. C., Jr., et al. 2003, PASP, 115, 928
———. 2007, ApJ, submitted
Kewley, L. J., & Dopita, M. A. 2002, ApJS, 142, 35
Kewley, L. J., Geller, M. J., Jansen, R. A., & Dopita, M. A. 2002, AJ, 124, 3135
Kobulnicky, H. A., & Kewley, L. J. 2004, ApJ, 617, 240
Kong, X., Charlot, S., Brinchmann, J., & Fall, S. M. 2004, MNRAS, 349, 769
Koorneef, J., & Code, A. D. 1981, ApJ, 247, 860
Landini, M., Natta, A., Salinari, P., Oliva, E., & Moorwood, A. F. M. 1984, A&A, 134, 284
Leger, A., & Puget, J. L. 1984, A&A, 137, L5
Leitherer, C., et al. 1999, ApJS, 123, 3
Li, A., & Draine, B. T. 2001, ApJ, 554, 778
———. 2002, ApJ, 572, 232
Lonsdale Persson, C. J., & Helou, G. X. 1987, ApJ, 314, 513
Madden, S. C., Galliano, F., Jones, A. P., & Sauvage, M. 2006, A&A, 446, 877
Martin, C. L. 1997, ApJ, 491, 561
Masegosa, J., Moles, M., & Campos-Aguilar, A. 1994, ApJ, 420, 576
Masters, K. L. 2005, Ph.D. thesis, Cornell Univ.
Mathis, J. S., Mezger, P. G., & Panagia, N. 1983, A&A, 128, 212
Mattioda, A. L., Allamandola, L. J., & Hudgins, D. M. 2005, ApJ, 629, 1183
Mayya, Y. D., & Prabhu, T. P. 1996, AJ, 111, 1252
Meurer, G. R., Heckman, T. M., & Calzetti, D. 1999, ApJ, 521, 64
Moustakas, J., Kennicutt, R. C., Jr., & Tremonti, C. A. 2006, ApJ, 642, 775
Osterbrock, D. E., & Ferland, G. J. 2006, Astrophysics of Gaseous Nebulae and Active Galactic Nuclei (2nd ed.; Sausalito: University Science Books)
Peeters, E., Spoon, H. W. W., & Tielens, A. G. G. M. 2004, ApJ, 613, 986
Perez-Gonzalez, P. G., et al. 2006, ApJ, 648, 987
Pety, J., Teyssier, D., Fossé, D., Gerin, M., Roueff, E., Abergel, A., Habart, E., & Cernicharo, J. 2005, A&A, 435, 885
Pilyugin, L. S. 2001, A&A, 374, 412
Pilyugin, L. S., & Thuan, T. X. 2005, ApJ, 631, 231
Prescott, M., et al. 2007, ApJ, in press (arXiv: 0706.3501v1)
Quillen, A. C., & Yukita, M. 2001, AJ, 121, 2095
Reach, W. T., et al. 2005, PASP, 117, 978
Regan, M. W., et al. 2004, ApJS, 154, 204
Rigby, J. R., & Rieke, G. H. 2004, ApJ, 606, 237
Rosa-Gonzalez, D., Terlevich, E., & Terlevich, R. 2002, MNRAS, 332, 283
Rosenberg, J. L., Ashby, M. L. N., Salzer, J. J., & Huang, J.-S. 2006, ApJ, 636, 742

Roussel, H., Sauvage, M., Vigroux, L., & Bosma, A. 2001, A&A, 372, 427
Rowan-Robinson, M., & Crawford, J. 1989, MNRAS, 238, 523
Salim, S., et al. 2007, ApJS, in press (arXiv: 0704.3611v2)
Sanders, D. B., Mazzarella, J. M., Kim, D.-C., Surace, J. A., & Soifer, B. T. 2003, AJ, 126, 1607
Sauvage, M., & Thuan, T. X. 1992, ApJ, 396, L69
Schlegel, D. J., Finkbeiner, D. P., & Davis, M. 1998, ApJ, 500, 525
Scoville, N. Z., Polletta, M., Ewald, S., Stolovy, S. R., Thompson, R., & Rieke, M. 2001, AJ, 122, 3017
Sellgren, K. 1984, ApJ, 277, 623
Sellgren, K., Luan, L., & Werner, M. W. 1990, ApJ, 359, 384
Sheth, K., Vogel, S. N., Regan, M. W., Teuben, P. J., Andrew, I., & Thornley, M. D. 2002, AJ, 124, 2581
Smail, I., Ivison, R. J., & Blain, A. W. 1997, ApJ, 490, L5
Smith, J. D. T., et al. 2007, ApJ, 656, 770
Sullivan, M., Mobasher, B., Chan, B., Cram, L., Ellis, R., Treyer, M., & Hopkins, A. 2001, ApJ, 558, 72
Surace, J. A., Sanders, D. B., & Mazzarella, J. M. 2004, AJ, 127, 3235
Tacconi-Garman, L. E., Sturm, E., Lehnert, M., Lutz, D., Davies, R. I., & Moorwood, A. F. M. 2005, A&A, 432, 91
Walter, F., et al. 2007, ApJ, 661, 102
Wang, B., & Heckman, T. M. 1996, ApJ, 457, 645
Wu, H., Cao, C., Hao, C.-N., Liu, F.-S., Wang, J.-L., Xia, X.-Y., Deng, Z.-G., & Young, C. K.-S. 2005, ApJ, 632, L79
Wu, Y., Charmandaris, V., Hao, L., Brandl, B. R., Bernard-Salas, J., Spoon, H. W. W., & Houck, J. R. 2006, ApJ, 639, 157